


REVIEW ARTICLE

Open Access



# All superconducting tokamak: EAST

Jiansheng Hu<sup>1\*</sup> , Weibin Xi<sup>1</sup>, Jian Zhang<sup>1</sup>, Liansheng Huang<sup>1</sup>, Damao Yao<sup>1</sup>, Qing Zang<sup>1</sup>, Yanlan Hu<sup>1</sup>, Guizhong Zuo<sup>1</sup>, Qiping Yuan<sup>1</sup>, Jinping Qian<sup>1</sup>, Zhiwei Zhou<sup>1</sup>, Xinjun Zhang<sup>1</sup>, Mao Wang<sup>1</sup>, Handong Xu<sup>1</sup>, Yahong Xie<sup>1</sup>, Zhengchu Wang<sup>1</sup>, Haiqing Liu<sup>1</sup>, Youwen Sun<sup>1</sup>, Liang Wang<sup>1</sup>, Guoqiang Li<sup>1</sup>, Hongxing Yin<sup>1</sup>, Yao Yang<sup>1</sup>, Xianzu Gong<sup>1</sup>, Kun Lu<sup>1</sup>, Guosheng Xu<sup>1</sup>, Junling Chen<sup>1</sup>, Fukun Liu<sup>1</sup>, Jiangang Li<sup>1</sup>, Yuntao Song<sup>1</sup> and the EAST team

## Abstract

Experimental Advanced Superconducting Tokamak (EAST) was built to demonstrate high-power, long-pulse operations under fusion-relevant conditions, with major radius  $R = 1.9$  m, minor radius  $a = 0.5$  m, and design pulse length up to 1000s. It has an ITER-like D-shaped cross-section with two symmetric divertors at the top and bottom, accommodating both single null and double null divertor configurations. EAST construction was started in 2000, and its first plasma was successfully obtained in 2006. In the past 15 years, plasma-facing components, plasma heating, diagnostics, and other systems have been upgraded step by step to meet its mission on exploring of the scientific and technological bases for fusion reactors and studying the physics and engineering technology issues with long pulse steady-state operation. An advanced steady-state plasma operation scenario has been developed, and plasma parameters were greatly improved. Meanwhile, front physics on the magnetic confinement plasmas have been systemically investigated and lots of fruitful results were realized, covering transport and confinement, MHD stabilities, pedestal physics, divertor and scrap-off layer (SOL) physics, and energetic particle physics. This brief review of EAST on engineering upgrading, stand-steady operation scenario development, and plasma physics investigation would be useful for the reference on construction and operation of a superconducting tokamak, such as ITER and future fusion reactor.

**Keywords** EAST, Superconducting tokamak, Magnetic confinement, Nuclear fusion

## 1 Introduction

The achievement of a steady-state operation with high performance is one major challenge for present-day tokamaks and future fusion devices. The steady-state operation of ITER will be the full non-inductive current-driven plasma with a pulse length of 3000s due to engineering limits. The demonstration of a steady-state scenario on current tokamaks needs a simultaneous integration of engineering technology and physical issues, such as external current drive, heat flux to the first wall and divertor, and active plasma control. As one of the superconducting fusion facilities,

the Experimental Advanced Superconducting Tokamak (EAST) is aiming to explore the scientific and technological bases for fusion reactors and to study the physics and engineering technology issues with long pulse steady-state operation [1–4].

EAST project was approved by the Chinese government in 1998 and started construction in Oct. 2000. The assembling was finished by the end of 2005 and the first commissioning started on Feb. 1, 2006, which finished on March 30, 2006, at the Institute of Plasma Physics, Chinese Academy of Sciences (ASIPP) [1]. Since then, EAST has been in operation for more than 15 years and achieved several milestones, in a steady-state scenario and H-mode plasma. The main design parameters of the EAST device are presented in Table 1 [2], and an overview photograph of the EAST device is shown in Fig. 1.

\*Correspondence:

Jiansheng Hu  
hujs@ipp.ac.cn

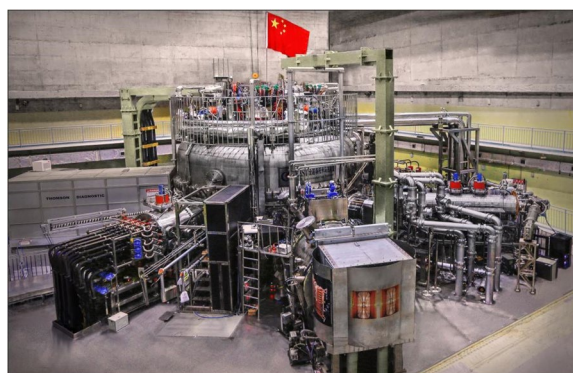
<sup>1</sup> Institute of Plasma Physics, Chinese Academy of Sciences, Hefei 230031, China



© The Author(s) 2023. **Open Access** This article is licensed under a Creative Commons Attribution 4.0 International License, which permits use, sharing, adaptation, distribution and reproduction in any medium or format, as long as you give appropriate credit to the original author(s) and the source, provide a link to the Creative Commons licence, and indicate if changes were made. The images or other third party material in this article are included in the article's Creative Commons licence, unless indicated otherwise in a credit line to the material. If material is not included in the article's Creative Commons licence and your intended use is not permitted by statutory regulation or exceeds the permitted use, you will need to obtain permission directly from the copyright holder. To view a copy of this licence, visit <http://creativecommons.org/licenses/by/4.0/>.

**Table 1** Main design parameters of the EAST device

Parameter	Performance
Major radius	1.88 m
Minor radius	0.45 m
Toroidal field	1.5–3.5T
Plasma current	1 MA
Elongation	$\text{Kappa} \leq 2$
Triangularity	$\delta \leq 0.7$
Available flux	$\Delta\Phi \approx 6.5 \text{ Vs}$

**Fig. 1** The overview photograph of the EAST device

EAST is aiming at the frontier of nuclear fusion energy research, to carry out joint experimental research on the basic physics and engineering problems of advanced tokamak fusion reactors with stable, safe, and efficient operation. It is to provide a scientific basis for the design and construction of nuclear fusion engineering test reactors and promote the development of other related disciplines and technologies in plasma physics [5]. EAST has three distinctive features: non-circular cross-section, fully superconducting magnets, and fully actively water-cooled plasma-facing components (PFCs), which will be beneficial to the exploration of the advanced steady-state plasma operation modes. Compared with the International Thermonuclear Experimental Reactor project (ITER), EAST is smaller but similar in shape and equilibrium, yet more flexible. Its construction and physics research will provide direct experience for ITER and China Fusion Engineering Test Reactor (CFETR) and will ultimately contribute to the development of fusion energy (<http://east.ipp.ac.cn>). Many experimental parameters obtained are close to the physical conditions required for the steady-state operation mode of the future reactor, which is a key step towards the experimental operation of future reactors. Up to the 2022 campaign, EAST has carried out over 118,824 shots (<http://east.ipp.ac.cn>). It is necessary to review EAST development and its physics

research. This paper briefly reviews engineering development and its current status of EAST in section 2, steady-state operation scenario development in section 3, and plasma physics investigation in 6 topics in section 4. The last is a summary.

## 2 EAST engineering development and current status

The main machine of the EAST device consists of six components, including an ultra-high vacuum chamber, toroidal coils, poloidal coils, thermal shields, external vacuum pumping, and a supporting system. The experimental operation also needs the support of large-scale cryogenic helium refrigeration, large-scale high-power pulse power supply and its loop, large-scale superconductor testing, large-scale computer control and data acquisition and processing, MW LHCD and RF wave heating, large-scale ultra-high vacuum, and a variety of advanced diagnostic measurement systems, etc. (<http://www.ipp.cas.cn/dakexuegongcheng/east/>).

### 2.1 EAST main machine

The EAST machine mainly consists of 14 superconducting poloidal fields (PF) coils and 16 superconducting toroidal fields (TF) coils, vacuum vessel (VV), thermal shields (TS), and cryostat vessel (CV). The 16 TF coils are arranged in a toroidal direction, its operating current is 14.3 kA, and the maximum toroidal magnetic field intensity at the center of the plasma can reach 3.5 T [6]. Six central solenoid coils and six large poloidal field coils form the poloidal field magnet system. The maximum operating current of PF is 14.5 kA, and the maximum poloidal magnetic field intensity and magnetic field change rate can reach 4.5 T and 7 T/s respectively [6]. The conductor used in the TF/CS/PF coils is an NbTi/Cu cable-in conduit (CIC) conductor, which is based on NbTi cooled with supercritical helium. The EAST main machine features a diameter of 7.7 m, a height of 10 m with a support frame and its total weight of 400 tons. The cutaway isometric drawing of the EAST main machine is as shown in Fig. 2 [7].

In addition, the auxiliary systems to maintain the operation of superconducting magnets include a superconducting feeder, PF power supply, TF power supply, and quench detection (QD) of the superconducting magnets system. Quench detection in superconducting magnet systems is distributed as follows over the 4 major sub-systems, including TF quench detection, PF and CS quench detection, quench detection in superconducting feeders, and electronic device for quench detection. In order to prevent electromagnetic perturbations caused by plasma scenarios and reduce false QDs, several novel compensation systems, such as a real-time feedback compensation

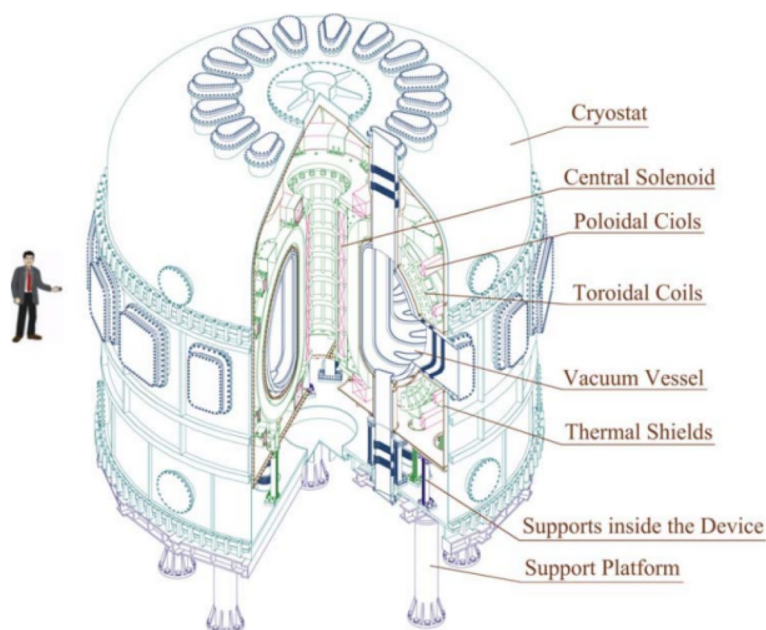


**Fig. 2** The cutaway isometric drawing of the EAST main machine

system to eliminate plasma-induced noise, pick-up coil-based detection system, RF noise suppression technology, have been developed to ensure the required fast response time for the QD system.

TF power supply provides a 15-kA current for TF coils, with the two-quadrant thyristor phase control AD/DC converter. The TF quench protection is composed of two DC breakers and one explosive breaker connected in series for TF coil quench discharge [8, 9]. PF power supply system has twelve sets of 15 kA four-quadrant thyristor phase control AD/DC converters, and the rated no-load voltage is from 350V to 1000V DC. Each PF power supply loop is connected to one set 2.4 kV/15 kA switch network unit for plasma initialization. And each PF coil is connected to one quench protection unit, which is composed of two DC breakers and one explosive breaker connected in series [10–13]. The PF coil power supply control system was updated from an analog control system to a full digital control system in 2015, to improve the power supply output linearity and accuracy, and to reduce the failure rate by an order of magnitude. The PF coil supplies PS11/12 were updated from thyristor phase control technology to the IGBT (Insulated Gate Bipolar Transistor) Pulse Width Modulation technology in Nov. 2022. This is the first time to use the PWM ac/dc converter to feed the PF coils in the Tokamak machine. The benefits of the new technology power supply are very low response latency, high voltage output efficiency, high power factor, and low harmonic wave, etc.

TF and PF magnets together generate a magnetic field to control plasma configurations. The vacuum vessel provides a high vacuum environment for high-temperature plasma operation [6, 14, 15]. Since 2006, it has been running safely and stably, and the false QDs during EAST operations is close to zero in the past 6 years.

Since 2006, the main technical upgrading of the EAST machine is as follows: firstly high-performance insulation breaks have been manufactured by vacuum winding technology to solve the vacuum leakage problem of original insulators after years of operation and have replaced all leaking insulation breaks in the cooling loops of magnets; secondly, with enough space for the upgrade in heating devices and diagnostic facilities, two cryostats which are installed in the 13 pairs of HTS current leads have been moved from the EAST machine hall to the new power supply hall which is about 30 m away from the EAST machine, two new feeder system have been developed. Now EAST machine has been running safely and stably for nearly 20 years.

## 2.2 Vacuum system

EAST vacuum systems as the basic configuration of the magnetic confinement fusion device mainly include a pumping system, fueling system, wall conditioning, measurement, and control system, which provide a good vacuum environment, clean wall condition, fuel injection, and particle exhaust and directly affect the quality of the high-temperature plasma.

When the EAST device was commissioned in 2006, a horizontal pump duct for the plasma vessel equipped with 4 sets of turbo molecular pumps with a total nominal pumping speed of  $12.9 \text{ m}^3/\text{s}$  and 4 cryo-pumps with a total nominal pumping speed of  $52 \text{ m}^3/\text{s}$  for  $\text{H}_2$  [16]. In addition, 2 and 4 cryo-pumps were installed at the bottom and top ports, respectively, connecting with the divertor region through tubes. Besides those outside pumps, two new dedicated inner cryopumps located at the outer target of low and upper divertors, respectively, had been mounted since 2008 for divertor pumping, with the calibrated pumping speed for  $\text{D}_2$  is about  $75 \text{ m}^3/\text{s}$ . In 2021, the pumping systems were upgraded. The turbo molecular pumps were changed into the magnetic molecular pump with a pumping speed of  $25 \text{ m}^3/\text{s}$ , and the number of outer cryopumps was increased to 14 sets. Furthermore, the part of the cryopump was upgraded into the pump with a larger pumping speed ( $18 \text{ m}^3/\text{s}$ ) and capacity ( $\sim 100 \text{ Pa} \cdot \text{m}^3$ ).

The fueling system is designed to meet the requirements of plasma fueling, wall conditioning, the radiative divertor, disruption mitigation, and diagnostic system. The injected gases include deuterium, helium, nitrogen, argon, and neon. In the first phase of the EAST machine, it designed 12 gas puffing systems for plasma fueling at top and bottom divertors. The piezo valves were used to control injection gas, but it has a long response time of 20–100ms for gas injection. Therefore, it is only used as a basic fueling technique to provide a working medium for plasma establishment, heating antenna, and divertor experiment, wall conditioning. In order to decrease the delay time of gas injection, 4 supersonic molecular beam injectors (SMBI), which could form supersonic speed gas with the theory speed of 400–1200m/s through a Laval nozzle and high-pressure gas, have been developed for the plasma density feedback and divertor heat flux control. The SMBI system has the EM valve response time of  $160 \mu\text{s}$  and a gas delay time of 5–25ms. The fueling efficiency of SMBI is about 30% in contrast to  $\sim 10\%$  with gas puffing. In order to further improve plasma fueling efficiency, 2 sets of pellet injection system (PI), which uses cryogenic liquid helium to cool gas into ice, form shot of specific size by cutting, and is accelerated and injected into the plasma by high-pressure gas, from mid-plane either at the high-field side or low-field side, and lower divertor, have also been developed in EAST machine. The results show the pellet fueling efficiency (max.  $\sim 50\%$  from high field side injection) is higher than SMBI and gas puffing. The wall condition system is designed for hydrogen removal or impurity suppression as well as to optimize wall conditioning for high-performance plasma operation.

The wall condition system includes baking, glow discharge cleaning (GDC) system, ion cyclotron cleaning system, and coating systems. The hot nitrogen is designed to bake the first wall, and right now, the common baking temperature of the first wall is limited to less than  $150 \text{ }^\circ\text{C}$  due to some engineering limits. And we have been developed 4 glow discharge cleaning systems and two RF discharge cleaning systems. The operation zone of GDC is the voltage of 100–500 V, and the current of 2–6A. The dedicated belt RF antenna has a wave frequency of 27/41 MHz and can produce max. power of 70 kW. It is noted that the RF cleaning system is compatible with a magnetic field, which is very important to be used to clean the first wall between the two shots in a future device. Boronization using carborane ( $\text{C}_2\text{B}_{10}\text{H}_{12}$ ) as the working material has been applied for wall conditioning from the first campaign of EAST. This technique has been demonstrated to suppress impurities and allow the attainment of low  $Z_{\text{eff}}$  plasmas in EAST. Unfortunately, it also introduces H to the walls, which leads to high particle recycling. Siliconization using  $\text{SiH}_4/\text{He}$  or  $\text{SiD}_4/\text{He}$  as working gases was also investigated on EAST [17]. It was found that siliconization could be used to reduce particle recycling slightly, but the H content reduction caused by  $\text{SiD}_4$  coating from  $\sim 28$  to  $\sim 8\%$  was slower than Li coating. Compared with traditional wall conditionings, Li coating was testified as the most effective way to suppress impurities, and reduce recycling and  $\text{H}/(\text{H}+\text{D})$  ratio to stabilize the plasma edge. Specifically, the high-Z tungsten core impurity concentration was maintained between 3 and 15 ppm during long H-mode plasmas [18].

With the help of these advanced vacuum pumping, fueling, and wall conditioning technologies, the vacuum vessel can provide enough and controllable pumping speed to achieve an ultimate vacuum lower than  $1.5 \times 10^{-6} \text{ Pa}$  with a water content of 2–5%.

### 2.3 Cryogenic system

The large-scale helium cryogenic system is one of the key subsystems for the EAST tokamak device, which is used for cooling of the cold components including the poloidal field (PF) and toroidal field (TF) coils, structures, thermal shields, buslines, HTS current leads, and cryopumps. The total cold mass is over 250 tons. The basic design capacity of the refrigerator is  $1050 \text{ W}/3.5 \text{ K} + 200 \text{ W}/4.5 \text{ K} + 13 \text{ g/s LHe} + 12\text{--}30 \text{ kW}/80 \text{ K}$ . And the security factor is 1.5. It is approximately equivalent to a helium refrigerator with a capacity of more than 2kW at 4.5 K. EAST cryogenic system is composed of compressors, oil removal systems, cold box, cryogenic distribution system, liquid helium Dewar, helium recovery, and storage system, purifier, etc. [19, 20].

EAST cryogenic system has served in the physical experimental campaigns for over 15 years since the first cool-down experiment in 2006. And its total operation time has been over 2000 days. In order to promote the refrigeration efficiencies and reliability, the EAST cryogenic system was upgraded gradually with new helium screw compressors and new dynamic gas-bearing helium turbine expanders with eddy current brakes to improve the original poor mechanical and operational performance from 2012 to 2015 [21]. And the helium gas purification system including the oil-removal system after the oil-injected screw compressors, the adsorbers inside the cold-box and two sets of external purifiers as well as the control system has been redesigned and reconstructed from 2019 to 2020, which was to avoid the fault of heat exchanger blocking due to the purity of gas helium [22]. At present, the EAST cryogenic system has performed 20 cool-down experimental campaigns till August 2022. And in the latest experiment, it has been operated continuously and stably for over 5 months. To ensure the future continuous 6 months of stable operation and promote the cooling capacity for the safety of superconducting

magnets, the 3.5K sub-cooling system upgrade will be considered in the future.

#### 2.4 Plasma facing components

As main plasma facing components (PFC), the divertor and first walls in EAST have been upgraded from full graphite to full metal with increasing heat removal capability step by step, as shown in Fig. 3. When the EAST device started operation in 2006, initial 500kA plasma was achieved using a non-actively cooled stainless steel plate as the sole plasma-facing material [23–25].

From 2008 to 2012, it was upgraded into doped graphite tiles (with SiC coating) bolted onto water-cooled heat sinks and used graphite paper as the interlayer to improve the mechanical connection between the tile and heat sink, whose capability of removing heat loads was up to  $2 \text{ MW/m}^2$  [26–28]. Then, the high field side, low field side, and passive plate were changed further from graphite tiles into molybdenum alloy in 2012, which successfully controlled the particle recirculation level of the first wall material [26, 29].

From 2014 to 2020, in order to obtain higher-parameter plasma, EAST developed a new type of W/Cu divertor

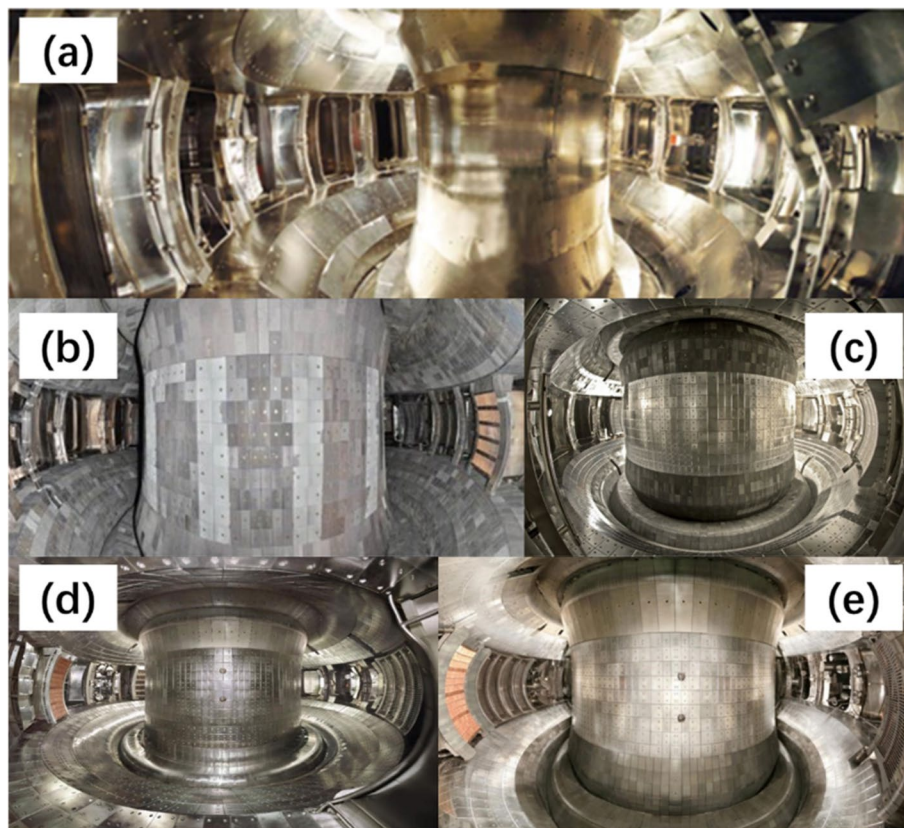


**Fig. 3** In-vessel view of PFC on EAST. **a** Full – SS for the first plasma. **b** Full carbon, 2008–2012. **c** Carbon divertor and TZM FW, 2012–2014. **d** W upper Div. & C lower Div. & TZM FW, 2014–2020. **e** W upper Div. & W lower Div. & TZM FW, 2020 to now

manufacturing technology for in-vessel components and successfully applied it to the EAST upper divertor, improving the heat transfer performance of the divertor PFCs, achieving heat removal capability up to 10 MW/m<sup>2</sup> and successfully obtaining a 100s H-mode plasma in 2017 [24]. In 2020, a full tungsten lower divertor has been developed, which has replaced the original graphite lower divertor and greatly improved the overall performance of the device [30]. The peak heat removal capacity is 10 MW/m<sup>2</sup> for a tungsten monoblock divertor and 20 MW/m<sup>2</sup> for a flat-type divertor [31, 32]. In 2021 with those tungsten divertors, EAST has successfully achieved plasma operation of 100 million degrees for 101s and long-pulse discharges up to 1056s [32].

### 2.5 Plasma heating and current drive

To improve plasma parameters and for non-inductive long plasma operation, plasma heating and current drive systems were greatly upgraded. Now, there are low hybrid current drive systems (LHCDs), ion cyclotron range of frequency (ICRF), electron-ion cyclotron range of frequency (ECRF), and natural beam injection (NBI) for plasma heating and current drive on EAST. The present distribution of EAST heating, pumping, and main diagnostics is shown in Fig. 4.

There are two LHCD systems working at continue wave mode with the parameters of 4MW/2.45GHz [33] and 6MW/4.6GHz [34], respectively. The 2MW/2.45GHz LHCD system [35] was built in 2007 with a Full Active

Multijunction (FAM) antenna and upgraded to 4MW in 2011 and Passive Active Multijunction (PAM) antenna in 2021 [36, 37]. The 6MW/4.6GHz LHCD system was completed in 2013 and put into an experiment in 2014. In order to realize the accurate control of loop voltage and  $\beta_p$ , the power control technology [38] is developed, which can realize the arbitrary waveform control of power. For the sake of studying the mechanism of LHW absorption and the ELM control, the power modulation technology [39] is realized, and the maximum modulation frequency is up to 100 kHz. LHCD power control provides important technical support for long pulse operation and physical experiment research.

The ion cyclotron range of frequency (ICRF) system at 25–70 MHz [40] has a capability of delivering more than 10 MW of RF power to the plasma for long pulse lengths up to 1000 s. The performance of ICRF heating has progressed steadily in the EAST. Initial ICRF experiments started in 2010 [41, 42]. The Hydrogen Minority Heating (H-MH) heating method has had the best plasma performance and has helped achieve H-mode by ICRF alone in 2012 [43]. The first successful application of the ICRF heating in the D (He3) plasma was also achieved. A new ICRF antenna with a lower parallel wave spectrum was fabricated and put into operation in the 2021 EAST experimental campaign. Significant progress has been achieved in H mode plasma with the new ICRF antenna on EAST [44].

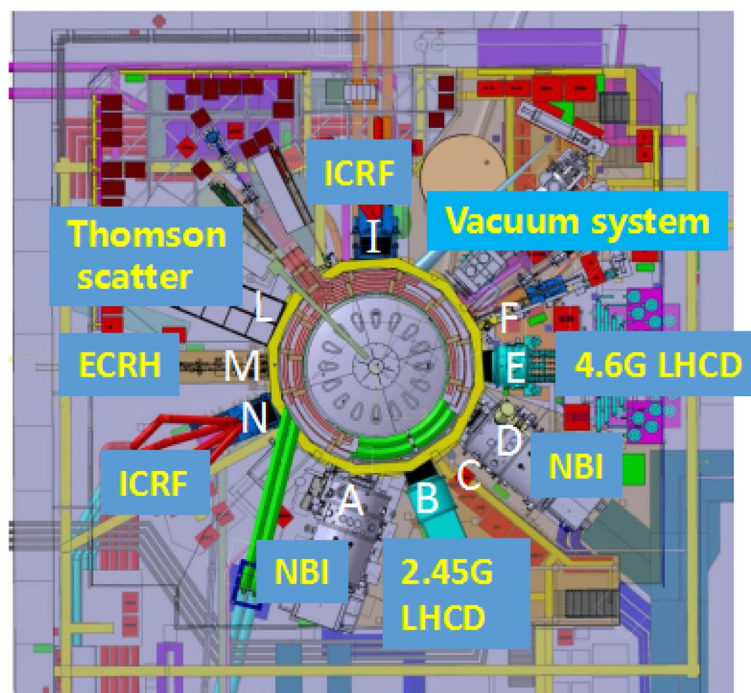


**Fig. 4** Distribution of EAST main systems

A long pulse electron cyclotron resonance heating (ECRH) system has been developed to meet the requirements of steady-state operation for EAST, and the first EC wave was successfully injected into plasma in 2015 [45]. The system is mainly composed of four 140 GHz gyrotron systems, 4 ITER-Like transmission lines, 4 independent channel launchers and corresponding power supplies, a water cooling, control, and inter-lock system, etc. The launcher has a main feature of active cooling in all mirrors which will ensure the availability of CW operation. Gycom gyrotrons are employed in the No. 1, No. 3, and No. 4 systems, and CPI gyrotrons are used in the No. 2 system. Since No. 1 gyrotron is under maintenance, the system has an available power of 2.05MW/1000s recently by using the remaining three gyrotrons. Some gyrotrons will be upgraded to dual frequency (140/105GHz) mode to fit low  $B_T$  (2.5T $\rightarrow$ 1.9T) operation in the future [46].

The NBI system was employed on EAST with two beamlines [47, 48]. The first beamline (NBI-1) was started in design and manufacture from the year of 2010, which was finished assembled and installed on the EAST in 2014 (co-injection). It injected the first neutral beam into the EAST plasma in the August of 2014 [49]. The second beam line (NBI-2) started manufacture in 2012 and finished in April 2015 and injected the first neutral beam in the same year too (counter-injection). According to the physical requirement, the NBI-2 was changed from counter-injection to co-injection in 2021 [50]. Each beamline was designed with a beam power of 4 MW and beam energy of 80 keV. In order to be operated with a long pulse, the real-time feedback control of the ion

source was applied and optimized [51]. Furthermore, a beam re-turn on technology, which is re-turn on the beam in several ms when the beam was terminated by break down or other reasons, such as the interference of the interlock system, was applied for NBI heating during the long pulse operation [52]. So, the NBI can be operated with a long pulse, the typical waveform can be seen in Fig. 5. For routine operation, the total injected power is around 3–5 MW and the beam pulse of 10 s. A long pulse of 100s with a beam power of 3 MW will be tested in the near future.

## 2.6 Diagnostics

After more than 10 years of development, nearly 80 diagnostics have been developed and implemented on the EAST, which are capable of measuring the dynamics of plasma profiles, instabilities, and plasma-wall interactions during long-pulse operation [53]. They are distributed on 12 different midplane ports and integrated with the machine and auxiliary heating systems, as shown in Fig. 6, Table 2.

All magnetic sensors have been installed in the vacuum chamber as an integral part of the in-vessel components, which can provide sufficient information about machine operation, plasma control, and physics analysis. The radial profiles of key plasma parameters, such as the contents of Te, ne, and Ti, along with the rotation, are available during the experiments. Thomson scattering (TS) systems can be used to determine the electron density ne and temperature Te with a time interval of 20ms [54, 55]. The advanced X-ray imaging crystal spectrometer

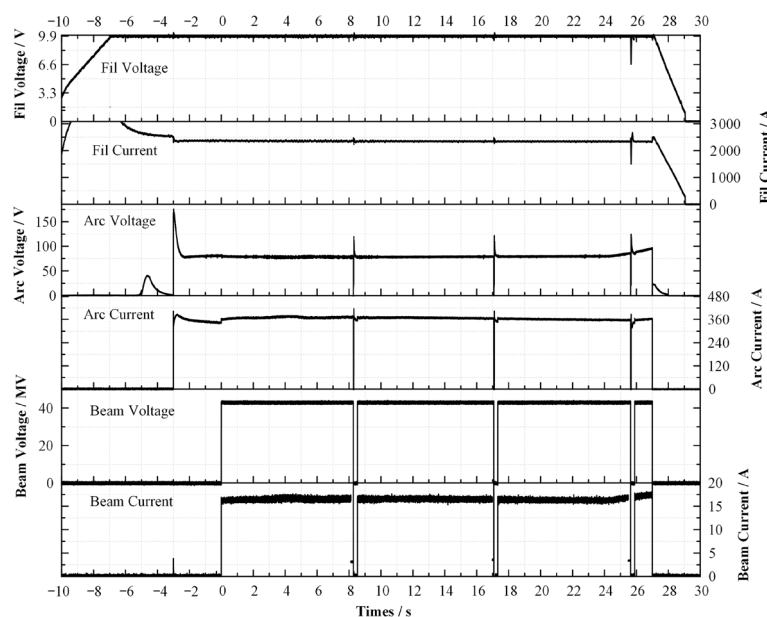


**Fig. 5** The typical waveform of long pulse operation with beam re-turn on technology

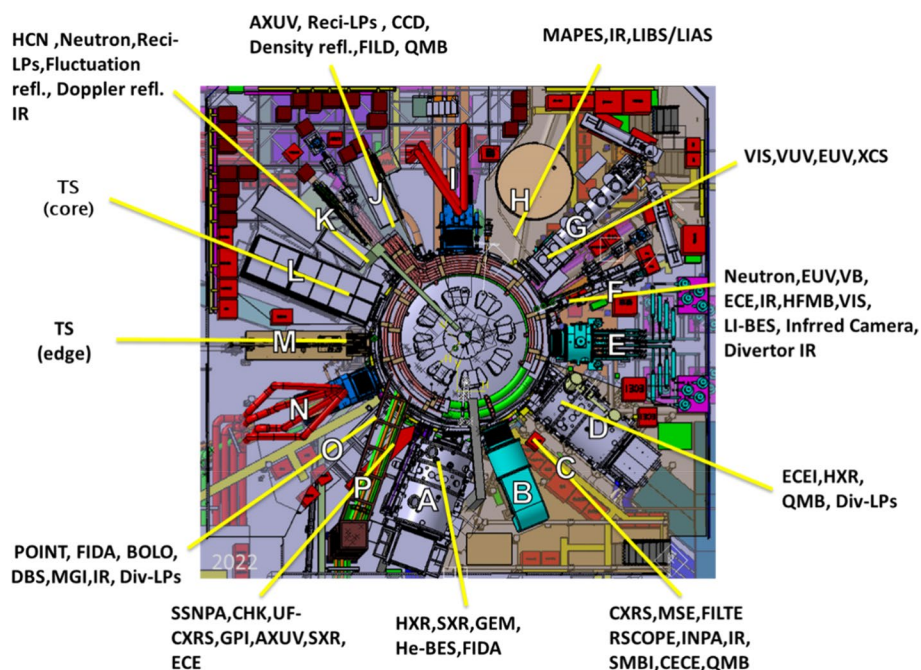


**Fig. 6** The layout of diagnostics on EAST. Nearly 80 diagnostics are distributed on 12 different midplane ports and integrated with the machine and auxiliary heating systems

(XCS), which can be used to record temporally and spatially resolved spectra of helium-like argon ions from multiple sight lines through plasma, is a powerful diagnostic tool for measurement of ion and electron temperature profiles as well as plasma toroidal rotation [56]. A fast-ion D-alpha spectrum (FIDA) has been developed to assess fast-ion behavior and energetic particle-related physics [57]. Particular attention has been paid to plasma core-edge diagnostics, such as lithium beam emission spectroscopy (Li-BES) to obtain edge electron density profiles [58]. An 11-chord, double-pass, radial viewing, and far-infrared laser-based polarimeter-interferometer (POINT) system has routinely operated for diagnosing the plasma current and electron density profiles during plasma discharge [59].

Based on the diagnostics mentioned above, an understanding of the high-performance long-pulse operation of the EAST is obtained, facilitating the design of the next-generation fusion reactors such as the ITER and CFETR.

### 2.7 Data acquisition and control

EAST CODAC, consisting of the central control system [60], data acquisition system [61], and data service system [62] as shown in Fig. 7, realizes the synchronization timing, coordinated communication, device and personal safety monitoring, and interlock protection of various

device plants, as well as data acquisition, storage, analysis, and visualization services to meet the requirements of the steady-state operation. EAST diagnostic data acquisition with more than 4000 channels is distributed around the EAST device, composed of more than 60 acquisition subsystems [63] with a sampling rate from 1Hz to 1GHz. The total data storage capacity is about 3000 TB with max data access bandwidth 10 GBytes/s.

Plasma control system (PCS) [64], which was transplanted from the DIII-D PCS infrastructure, has the capability of realizing advanced configuration, profile, and heat load control after more than 10 years of continuous upgrading and development [65–69]. As a tokamak with a vertically elongated cross-section, the EAST PCS is required to have the ability to stabilize the vertical instability. Numbers of vertical feedback control algorithms have been designed and implemented [70–72] in EAST PCS, which extended the EAST operation region and improved the stability, providing an important reference scheme for future fusion reactor design.

The precision and speed of real-time equilibrium reconstruction are related to the plasma control performance. With the parallelized Grad-Shafranov solver and middle-scale matrix calculation modules on GPU, a new reconstruction code called P-EFIT was developed [12], which reproduces the EFIT reconstruction algorithms at a fraction of the EFIT computational time [73–75].



**Table 2** The diagnostic systems in EAST

No.	Port	Abbreviations	Detail
1	A	HXR	Hard X-ray
2		SXR	Soft-X ray
3		GEM	Gas electron multiplier
4		He-BES	Helium beam emission spectroscopy
5		FIDA	Fast-ion D-alpha
8	C	CXRS	Charge exchange recombination spectroscopy
9		MSE	Motional stark effect
10		FILTERSCOPE	Filterscope
12		INPA	Imaging of neutral particle analyser
13		IR	InfraRed
14	D	SMBI	Supersonic molecular beam injection
15		CECE	Correlation electron cyclotron emission
16		QMB	Quartz crystal microbalance
17		ECEI	Electron cyclotron emission imaging
18		HXR	Hard X-ray
19		QMB	Quartz crystal microbalance
20		Div-LPs	Divertor Langmuir probes
21	F	Neutron	Neutron
22		EUV	Extreme ultraviolet
23		VB	Visible Bremsstrahlung emission
24		ECE	Electron cyclotron emission
25		IR	InfraRed
26		HFMP	High-frequency magnetic perturbation
27		VIS	Visual inspection system
28		LI-BES	Lithium beam emission spectroscopy
29	G	Infrared Camera	Infrared camera
30		Divertor IR	Divertor infrared
31		VIS	Visual inspection system
32		VUV	Vacuum ultraviolet imaging system
33	H	EUV	Extreme ultraviolet
34		XCS	X-ray imaging crystal spectrometer
35		MAPES	Material and plasma evaluation system
36		IR	InfraRed
37		LIBS/LIAS	Laser-induced breakdown spectroscopy/laser-induced ablation spectroscopy
38	J	AXUV	Absolute extreme ultraviolet spectroscopy
39		Reci-LPs	Reciprocating Langmuir probes
40		CCD	Charge-coupled device
41		Density refl.	Density reflectometer
42		FILD	Fast ion loss detector
43	K	QMB	Quartz crystal microbalance
44		HCN	Hydrogen cyanide
45		Neutron	Neutron diagnostic
46		Reci-LPs	Reciprocating Langmuir probes
47		Fluctuation refl.	Fluctuation reflectometer
48	L	Doppler refl.	Doppler reflectometer
49		IR	InfraRed
50	L	TS (core)	Core Thomson scattering
51	M	TS (edge)	Edge Thomson scattering

**Table 2** (continued)

No.	Port	Abbreviations	Detail
52	O	POINT	Polarimeter-interferometer
53		FIDA	Fast-ion D-alpha
54		BOLO	Bolometer
55		DBS	Doppler backscattering
56		MGI	Massive gas injection system
57		IR	InfraRed
58		Div-LPs	Divertor Langmuir probes
59	P	SSNPA	Solid state neutral particle analyzer
60		CHK	Cherenkov
61		UF-CXRS	Ultra-fast charge exchange recombination spectroscopy
62		GPI	Gas puff imaging
63		AXUV	Absolute extreme ultraviolet spectroscopy
64		SXR	Soft-X ray
65		ECE	Electron cyclotron emission

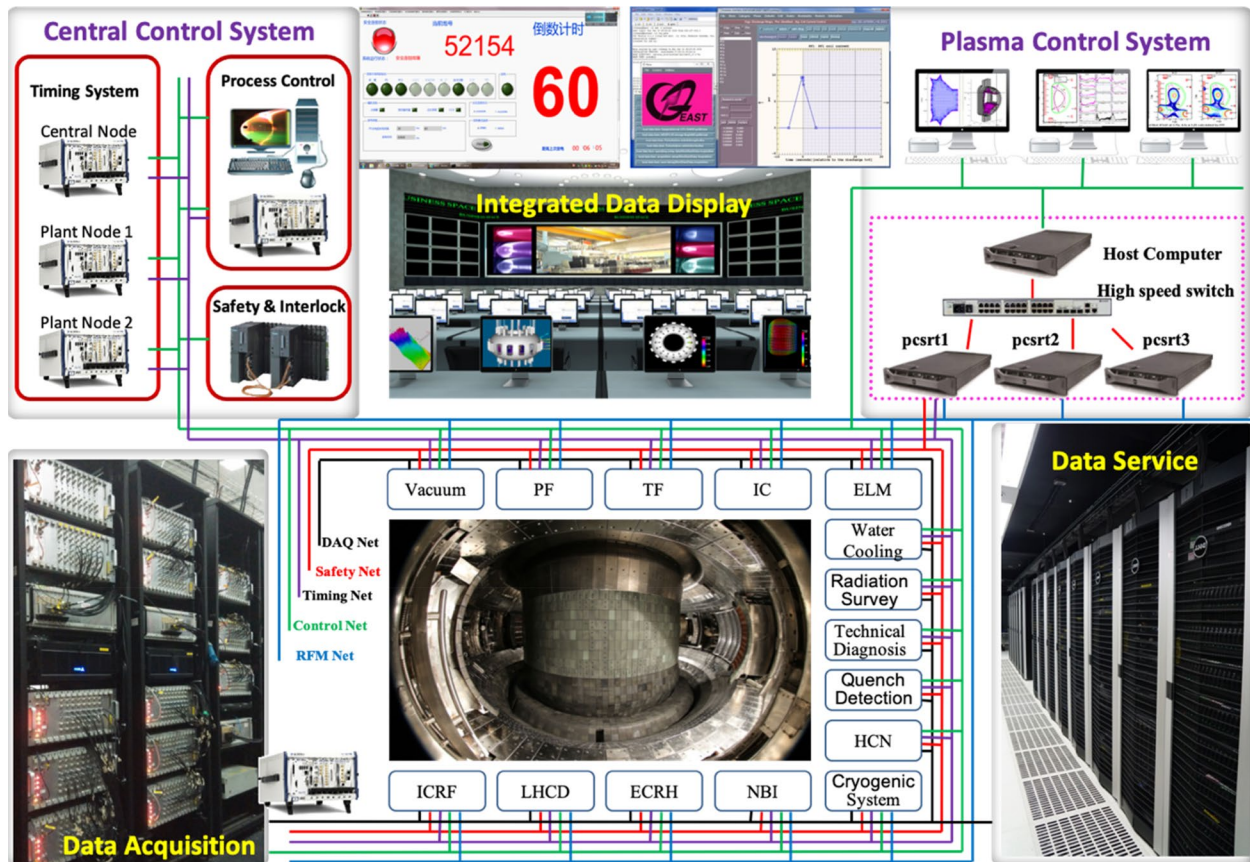


**Fig. 7** Block diagram of EAST CODAC and plasma control system

Integrated into the EAST plasma control system, P-EFIT not only provides control signal results but also enhances EAST plasma control capacity with dedicated function modules [76, 77].

Some new control techniques for steady-state operation have been developed in EAST PCS [78]. The pre-calculated linear drift rate for each integrator channel is pre-calculated each day according to a routine

hundred-seconds test shot for integrators, which is subtracted from raw data in PCS to eliminate the impact of linear drift during plasma discharges. For high-performance and non-inductive plasma operations, the plasma beta and loop voltage control have been implemented in PCS. In addition, a data segment archiving technology of MDSplus was applied to save all data in segments without increasing the computer memory or reducing the saving frequency.

In conclusion, EAST CODAC and PCS systems provide an effective control guarantee for EAST’s thousand-second operation and achievement of excellent experiment results.

### 3 Scenario development on EAST

As a long-term goal, the EAST program is to provide a suitable platform to address physics and technology issues relevant to develop high-performance H-mode plasmas. Significant progress has been made in developing scenarios contributing to ITER baseline, hybrid, and steady-state scenarios, together with helium H-mode plasmas.

#### 3.1 Achievement of long-pulse divertor operation

As a superconducting tokamak, the main mission of EAST is to demonstrate high-power, long-pulse operations under fusion-relevant conditions. In the past 15

years, focusing on long pulse divertor operation, plasma duration was extended, as well as the improvement of plasma parameters, as shown in Fig. 8. And parameters in typical long pulse plasmas are listed in Table 3.

Long pulse operation over 410s [79] has been achieved in the campaign 2012, which was driven by LHCD. The LHCD power was feedback controlled by a flux loop to minimize the poloidal flux consumption and maintain the plasma current. The plasma configuration was varied from USN via DN to LSN during the discharge with strike point sweeping to improve power handling at the divertor target plates, minimizing divertor heat load, impurity influxes, and plasma-wall interactions. In addition, all PF coil currents at a minimum level (<2 kA) were well controlled away from the coil current limitation to maintain a large safe operation margin for superconducting coils.

A steady-state long pulse with a duration over 100 s and a core electron temperature over 10 keV was achieved established and stably sustained by applying both lower hybrid wave (LHW) and on-axis electron cyclotron resonance heating (ECRH) in the middle of 2021 [80]. It was found a reduction of core turbulence by multi-scale instabilities interaction with MHD and steep central electron temperature gradient region. In this kind of plasmas with a high central electron temperature gradient (ETG), the turbulence-driven current

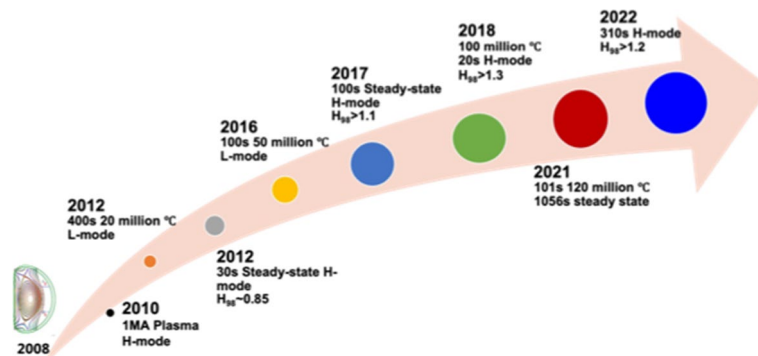


Fig. 8 Experiment milestones of long pulse divertor operation in EAST

Table 3 Parameters in typical long pulse plasmas in EAST

Shot	Year	Ip (MA)	Pulse length (s)	<ne> (10 <sup>19</sup> /m <sup>3</sup> )	H/L mode	H&CD (MW)	Ti (keV)	Te (keV)	τ <sub>e</sub> (s)	β <sub>N</sub>
43,336	2012	0.27	410	1.0	L	1.2	0.8	/	0.038	/
41,195	2012	0.27	31	2.5	H	2.8	0.9	/	0.04	/
73,999	2017	0.4	101	3.0	H	3.0	1.1	5.0	0.056	0.9
90,949	2019	0.35	60	4.3	H	3.4	1.0	5.5	0.06	1.6
106,915	2021	0.33	1056	1.8	L	1.6	0.8	6.5	0.06	0.9
110,488	2022	0.3	310	3.2	H	4.8	1.0	6.0	0.045	1.6

has been experimentally observed and the ratio of the turbulent current to the total current can reach a maximum of 5% (25% of the bootstrap current) at the  $q=1$  rational surface [81]. Those experimental observations on EAST suggest the interaction among the ETG turbulence, the turbulent current, and the  $m/n=1/1$  kink mode plays a contributing role in sustaining the stationary high- $\beta_{\theta e}$  long pulse plasmas. Power balance analysis shows that the increase of ECRH power can increase the normalized  $T(e)$  gradient significantly at the plasma core region ( $\rho < 0.6$ ), but does not change the  $T(e)$  profile stiffness in the low-density L-mode plasmas [82].

Recently near the end of 2021, a steady-state plasma with a world-record pulse length of 1056 s was obtained, where the density and the divertor peak heat flux were well controlled, with no core impurity accumulation. It is a fully non-inductive plasma with dominant e-heating zero injected torque with a total injected energy of 1.73GJ. The plasma current is mainly driven by LHCD and a moderate bootstrap current ( $\sim 37\%$ ). A new high-confinement and self-organizing regime was discovered and demonstrated. The plasma regime ( $H_{98} \sim 1.2$ ,  $\beta_p \sim 1.5$ ), the so-called Super I-mode, is characterized by the coexistence of an electron ITB (eITB) at the plasma center and an improvement energy confinement mode (I-mode), without ELMs, at the plasma edge, leading to a large improved energy confinement. The confinement time  $\tau_E$  is higher than the value predicted by the H-mode scaling law by 20% [83].

### 3.2 Achievement of long pulse H-mode plasmas

The first long pulse H-mode around 32 s with a combination of LHCD and ICRH has been achieved in the EAST experimental campaign of 2012 [79]. This is about 10–20 times longer than the present diffusion time, thus setting a record for the longest H-mode duration at that time. These long H-mode plasmas, achieved with extensive Li wall coating, are highly reproducible, with the heating power  $P_{\text{LHCD}}=1\text{--}2$  MW and  $P_{\text{ICRH}} = 0.5\text{--}1.5$  MW, which is about 1–3 times the threshold power for the transition from the usual low confinement mode, L-mode, to H-mode double null divertor configuration. In those shots, the toroidal magnetic field was 1.9T, plasma current was 280kA, plasma density was  $0.5n_{\text{GW}}$ ,  $q_{95}$  was about 6.8,  $\delta$  was 0.5,  $\kappa$  was 1.7, and  $q_{95}$  was 6.8. It was discovered that LHCD induces a profound change in the magnetic topology of the edge plasma by driving helical current filaments on the magnetic field lines in the boundary, leading to a three-dimensional distortion of the edge magnetic topology. These small ELMs are with a frequency of 0.5–1 kHz and peak heat fluxes on the PFCs from the plasma ejected by the small ELMs are largely below  $2 \text{ MW/m}^{-2}$ . This small-ELMy H-mode regime

exhibits a confinement quality modestly lower than the standard ELMs, with a confinement enhancement factor,  $H_{98(y;2)} \sim 0.9$ . However, this H-mode plasma discharge is not fully non-inductive and its duration is limited by the available flux of the PF coils and by wall particle saturation. Several upgrades on EAST were applied to extend long-pulse H-mode discharges, including active divertor pumping using the internal toroidal cryopump, installation of a tungsten divertor, augmented heating, and current drive capabilities.

In 2014, the long pulse H-mode performance has been enhanced. A 28 s long-pulse H-mode [84] was obtained with the newly implemented 4.6 GHz LHCD system with  $H_{98} \sim 1.2$ , exceeding the 32 s H-mode ( $H_{98} \sim 0.9$ ) in 2012. An important factor for achieving the 28 s high-performance H-mode is the high triangularity,  $\delta \sim 0.55$ , and high density ( $n_e/n_G \sim 0.55$ ). The divertor peak heat flux was controlled largely below  $3 \text{ MW/m}^{-2}$ , resulting from type-II like small ELMs.

After the commissioning of the tungsten divertor and redesigned mono-block units [85] with improved heat transfer in 2015, world records of over 60 s and 100 s [53, 86]. H-mode operation with strike points on the tungsten divertor was obtained. The steady-state scenarios were characterized by fully non-inductive current drive (zero loop voltage) and high-frequency small-amplitude ELMs, and it verified the stable control capability of heat and particle exhausts using the ITER-like tungsten divertor. Using  $\sim 3.4$  MW of total injected RF power for heating and current drive, the first long pulse H-mode (61 s) with zero loop voltage and an ITER-like tungsten divertor has demonstrated access to broad plasma current profiles by increasing the density in fully noninductive lower hybrid current-driven discharges. These long pulse discharges reach wall thermal and particle balance and exhibit stationary good confinement ( $H_{98y2} \sim 1.1$ ) with low core electron transport. Small and rapid ELMs are with a frequency of 100–200 Hz, and the stationary safety factor profile has a minimum value  $q_{\text{min}} \sim 1.5$ . The tungsten divertor temperature remains constant at about  $500 \text{ }^\circ\text{C}$  with a constant peak heat flux of  $\sim 3.5 \text{ MW m}^{-2}$ , showing that the divertor has reached thermal equilibrium. The first demonstration of a  $>100$  s time scale long-pulse steady-state scenario was also achieved with a good plasma performance ( $H_{98(y2)} \sim 1.1$ ) and a good control of impurity and heat exhaust with the upper tungsten divertor. The RF power heating and current drive (H&CD) has a total of  $\sim 0.5$  MW lower hybrid wave (LHW) at 2.45 GHz,  $\sim 1.7$  MW LHW at 4.6 GHz,  $\sim 0.4$  MW ECH, and  $\sim 0.5$  MW ICRF. This long-pulse discharge reaches wall thermal and particle equilibrium, with the steady-state peak heat flux on the divertor plates being maintained at  $\sim 3.3 \text{ MWm}^{-2}$  and the particle

exhaust rate being maintained at  $\sim 6.6 \times 10^{20} \text{ D s}^{-1}$ . It was found that a gradual increase of loop voltage after 90 s causes by the ECRH protection of the cutoff, which suggests that ECH has the effect on the avoidance of impurity accumulation.

EAST experiment has also demonstrated a long pulse steady-state high plasma performance scenario with core-edge integration in 2018. A discharge with a duration over 60 s with  $I_p \sim 0.35 \text{ MA}$ ,  $\beta_p \sim 2.0$ ,  $\beta_N \sim 1.6$ ,  $H_{98} \sim 1.3$ , and internal transport barrier on electron temperature channel is obtained with multi-RF power H&CD. Small ELMs with the frequency of 100–200 Hz were obtained in this long pulse H-mode discharge. Optimization of plasma shape and local gas puffing located close to the LHW antenna were investigated to maintain RF power coupling and to avoid the formation of hot spots on the LHW antenna. The on-axis ECH was applied for the core electron heating and the control of high Z impurities.

Parallel to long pulse H-mode operations, the development and test of possible scenarios for steady-state advanced tokamak, i.e., the research on the extension of high  $\beta_p$  regime towards higher bootstrap current fraction, were carried out. An example of EAST high  $\beta_p$  discharge using pure RF H&CD was achieved with parameters of  $\beta_p \sim 2.0$ ,  $\beta_N \sim 1.6$ ,  $f_{bs} \sim 50\%$ ,  $f_{GW} \sim 0.8$ , and  $H_{98Y2} > 1.3$  at  $q_{95} = 6.7$ , which close to the design target of the CFETR Phase-III 1 GW fusion power operation scenario [87, 88]. More data analysis shows improved confinement and reduced turbulence when extending to higher  $\beta_p$ . The higher  $\beta_p$  with high energy confinement was observed in plasmas with higher density. By tailoring the current density profile, a  $q$ -profile with local (off-axis) negative shear is achieved, which yields improved confinement and MHD stability. Transport analysis and simulation suggest that the combination of a high-density gradient and high Shafranov shift allows turbulence stabilization and higher confinement.

Recently in 2022, a long fully noninductive high beta H-mode scenario ( $H_{98Y2} > 1.3$ ,  $\beta_p > 2.5$ ,  $f_{Gr} > 0.6$ ,  $f_{bs} \sim 49\%$ ) with small ELMs was achieved with active controls of the stationary and transient divertor heat and particle fluxes. Compared to the longest H-mode achieved in 2017, the new record not only extended the plasma duration from 101 s to more than 300 s, but also improved plasma parameters, i.e.,  $\beta_p$ ,  $\beta_N$ ,  $f_{bs}$ ,  $H_{98}$ , and  $ne/n_{GW}$  (not published).

### 3.3 Development of low $q_{95}$ H-mode plasmas

In the recent EAST experiments, an effort has been made to explore high-performance stable plasma operation at a low  $q_{95}$  ( $q_{95} < 3.5$ ) regime that could demonstrate future ITER baseline scenarios and contribute to understand its relevant physics issues. The discharges at  $q_{95} < 3.5$  regimes have been achieved with the quasi single-null

divertor configuration at an unfavorable BT direction. The resonant magnetic perturbation (RMP) coil with toroidal mode number  $n = 4$  was used to control high-Z impurity accumulation and to mitigate low-frequency large ELMs. Statistic result indicates that improved confinement and the formation of internal transport barrier in ion thermal channel strongly correlates to the excitation of fishbone.

Extensive experiments of hybrid scenario development [89] have also been carried out on EAST tokamak recently with the ITER-like tungsten divertor. The  $\beta_N$  in this operational scenario is intermediate up to 2.1 with  $q_{95} = 3.7$ . The internal transport barrier (ITB) was frequently observed with the central flat  $q$  profile, and it was found that the fishbone mode ( $m/n = 1/1$ ) can be beneficial to sustain the central flat ( $q_{(0)} \sim 1$ )  $q$  profile; thus, a stable ITB can be obtained for better plasma performance. The formation of the ITB of the electron density is related to the fishbone activities. Energy transport analysis shows that the fishbone instabilities have a suppression on electron turbulent energy transport, while the ITB of ion temperature is due to the suppression of high-k modes (electron temperature gradient).

### 3.4 Demonstration of helium H-mode plasma with pure RF power

To support the ITER non-nuclear operational phase, helium experiments have been investigated in EAST with the ITER-like Tungsten divertor. The concentration of helium [90] is found to be a key parameter in H-mode operation. The higher helium concentration increases the L-H transition power threshold and degrades the energy confinement. The global energy confinement time in He plasmas was on average about 30% lower than in  $\text{D}_2$  plasmas.

## 4 Physics research in support of future fusion reactors

### 4.1 Transport and confinement

#### 4.1.1 Electron heat transport

Non-local heat transport has been observed and studied in EAST ohmic plasmas [91]. The non-local heat transport occurs with electron density  $n_{e0}$  below a critical value of  $(1.35 \pm 0.25) \times 10^{19} \text{ m}^{-3}$  and plasma current  $I_p = 450 \text{ kA}$ . The electron density fluctuation in the plasma core starts to increase within 5 ms after SMBI, while the response time of core electron temperature and density is about 15 ms. The results imply that the turbulence intensity was not only determined by the local gradients. Also, intense intermittent radiation has been observed regularly in EAST plasmas [92]. The duration of radiation bursts is with a characterization time of a few microseconds, and the radiation frequency  $f$  is at the plasma frequency, and the frequency bandwidth  $\Delta f$  is very narrow ( $\sim 1.5 \text{ MHz FWHM}$ ,  $\Delta f/f \sim 3 \times 10^{-5}$ ). The fine structure of the

spectrum in the frequency domain has been observed, and the cavity modes model is capable of explaining the radiation frequency and the frequency spacing.

High- $\beta_p$  plasmas with steep central electron temperature gradients have been achieved by ECH and LHCD on EAST. An intrinsic current is observed to be modulated by turbulence driven by the electron temperature gradient [81]. This turbulent current is generated in the counter-current direction and can reach a maximum ratio of 25% of the bootstrap current. The dominant mechanism for the turbulent current generation is due to the divergence of ETG-driven residual flux of current. The maximum values of turbulent current and electron temperature gradient lead to the destabilization of an  $m/n=1/1$  kink mode, which by counteraction reduces the turbulent level ( $m$  and  $n$  are the poloidal and toroidal mode numbers, respectively). The observations suggest that the self-regulation system including turbulence, turbulent current, and kink mode is a contributing mechanism for sustaining the steady-state long-pulse high- $\beta_{0e}$  regime.

#### 4.1.2 Particle confinement and transport

For particle transport investigation, a density modulation is a powerful tool. On EAST tokamak, SMBI density modulation experiments have been conducted in different confinement regions [93]. This technique has also been used in RMP ( $n = 2$ ) induced density pump-out discharges with NBI-heated H mode [94], and the results showed that the diffusive coefficient becomes larger and the inward convection velocity decreases towards the plasma edge after applied RMP switched on.

For high-density operation, pellet injection is a necessary method in the future tokamak, such as ITER. EAST has been equipped with a 10-Hz deuterium pellet injection system and high-density operation approaching the Greenwald density limit ( $\sim 0.84n_{GW}$ ) with MARFE movement has been investigated [95]. In RMP-induced density pump-out discharges with similar shapes to those in ITER with  $q_{95} \sim 3.8$ , and triangularity  $\delta \sim 0.45$ , pellet fueling with a frequency of 5 Hz from  $\sim 40$  cm above the mid-plane on the low field side is also used to compensate the decreased density and stored energy [96].

#### 4.1.3 Momentum transport and intrinsic rotations

The application of low-hybrid waves to EAST L-mode plasmas has been observed to induce notable increments in co-current plasma rotation from XCS diagnostic [97], in the absence of any other discernible external torque inputs [98]. Specifically, co-current changes in the toroidal rotation of up to 40 km/s in the core region and 20 km/s in the edge have been documented in early experiments at EAST, where low-hybrid current drive (LHCD) was applied in L-mode ohmic plasmas.

The ICRF-induced rotation increments, with about a 15 km/s difference in co-current direction, have been observed when the magnetic configuration changes from lower-single-null to double-null. Both discharges were heated by 27 MHz ICRF with the same  $I_p = 0.5$  MA, the same density ( $ne \sim 1.75 \times 10^{19} m^{-3}$ ), toroidal magnetic field ( $Bt = 2.0$  T), and similar RF power ( $P_{RF} = 1.75$  MW). The result implies the effects of edge scrape-off layer flows on the core plasma rotations [99].

The dimensionless analyses of LHCD and ICRF plasmas, as reported in reference [100], demonstrate that the increments in rotation are proportional to the negative changes in internal inductance following the injection of radio frequencies. This finding provides supplementary evidence in support of the Mach number scaling principle, as proposed in reference [98], which posits a correlation between toroidal rotation velocities and current density profiles, specifically predicting greater increments in rotation for flatter current density profiles.

#### 4.1.4 Impurity transport

Based on the development of the high-performance high-Z impurity diagnostics [101–103], the behavior of high-Z impurity in different plasma scenarios and the effect of real-time wall conditioning of lithium granule injection, RMP, and on-axis RF heating on the core tungsten suppression have been experimentally studied [104–106]. As a result, the effect on suppression of impurity source, enhancement of impurity screening in the edge, and control of tungsten content in core plasma has been verified, respectively.

The integral modeling workflow under the OMFIT framework is used to study the tungsten transport, and the result indicates the tungsten accumulation in the NBI dominant-heated high  $\beta_N$  scenario is caused by a large neoclassical pinch, which may be originated in density peaking and an enhancement of toroidal rotation [107]. On the other hand, for high-performance fully non-inductive discharge in EAST, high  $T_e$  and its gradient by on-axis ECRH play a key role to generate large turbulent diffusion through increasing the growth rate of linear instability so that tungsten accumulation is prevented [108]. With strong support from experimental study and physical understanding of tungsten transport, reproducible long-pulse high  $\beta_p$  H-mode discharges with tungsten concentration at  $\sim 10^{-5}$  were successfully achieved with stable tungsten control approaches of real-time wall conditioning and on-axis ECRH.

## 4.2 MHD and 3D physics

### 4.2.1 Core MHD

In the observation of MHD instabilities, modes associated with internal kink modes such as snake, saturated helical  $m/n=1/1$  mode, and sawtooth are of particular

interest. Firstly, two typical snake oscillations were observed in EAST experiments. One of the snake oscillations disappeared before the sawtooth crash [109], while the other coexisted with the sawtooth crash [110]. Secondly, the saturated helical mode was first observed in both high  $\beta_p$  [111] and high electron temperature  $T_e$  [112] hybrid scenarios on EAST. Active control of sawtooth has been demonstrated on EAST by varying the electron cyclotron current drive (ECCD) injection angles in real time [113].

Real-time control of tearing mode (TM) or neoclassical tearing mode (NTM) is an important topic and needs to be further verified and studied. NTM control system was developed on EAST in 2015 [114, 115]. TM/NTM suppression by electron cyclotron waves (ECW) has been studied on EAST since 2015 [116]. At the same time, a comparison with the numerical simulation has been carried out [117–120]. The modified Rutherford equation is used for experimental data analysis, and its comparison with the numerical simulation has been done [117]. Simple relations are found between the minimum ECW power and the plasma and wave parameters, which can be used to predict the ECW power for mode stabilization. It is demonstrated that a threshold in ECW power for disruption avoidance exists by stabilizing the magnetic island with ECCD, and its reason is given by analyzing the modified Rutherford equation [118]. The diffusivity of fast electrons is found to degrade the efficiency of NTM stabilization by ECCD by 2-3 times for modulated current drive [119], which will have a great impact on the NTM suppression system in ITER. In addition, new control strategies are being explored to improve the efficiency of NTM stabilization by ECCD, including utilizing the resonant magnetic perturbations to make magnetic islands rotate non-uniformly [120].

Error fields are more sensitivity for future reactors. Error field locked mode can limit the high-performance operation and even lead to disruption. Therefore, clarifying its scaling differences between theory and experiment is significant. The spectrum effect for  $n=1$  RMP field penetration has been studied and demonstrated the importance of plasma response on determining the threshold RMP current in this process [121]. The observed around square root density scaling in EAST agrees well with the fluid theory, when all parameters were determined experimentally, especially the observed energy confinement scaling (close to in Ohmic SOC regime) rather than the Neo-Alcator was used for the estimation of momentum diffusion time [122]. This provided a good validation of fluid field penetration theory and solved the longstanding discrepancy between field penetration scaling observation and theory. A similar scaling in RF heating plasmas was obtained. It agrees well with MHD field penetration theory and modeling results [123]. The penetration dependence on toroidal field strength and  $q_{95}$  has been further studied experimentally and agrees well with the theory [124]. Further, to have a better connection with ELM control, the penetration of  $n=2$  RMPs has also been studied in detail [125]. It was again demonstrated that the penetration threshold depends on the RMP field taking into account plasma response. An interesting nonlinear mode coupling between the penetrated  $n=2$  mode and an  $n=1$  mode has been directly observed. This is potentially important for understanding the nonlinear coupling effects in RMP ELM suppression.

**4.2.2 RMP controlling ELM**

A set of in-vessel RMP coil systems has been installed in EAST in 2014 for ELM control, as shown in Fig. 9 [126, 127]. It consists of  $2 \times 8$  coils with up and down

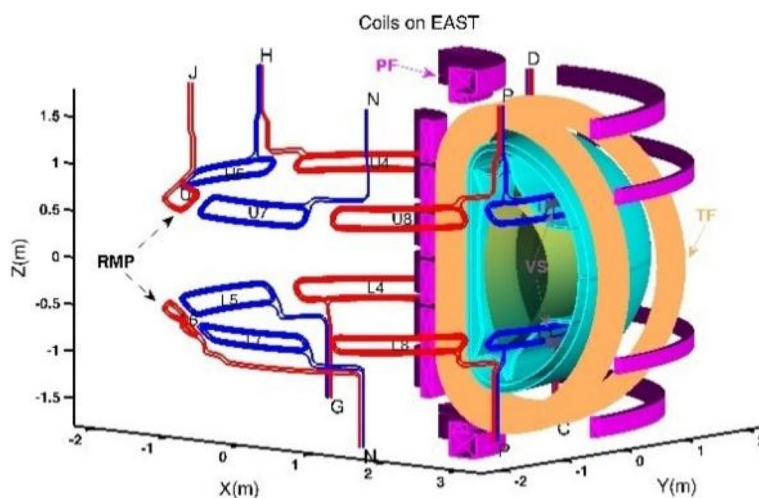


**Fig. 9** RMP coils in the EAST tokamak (From Ref [119])

symmetry located at the upper (U) and lower (L) parts of the last closed flux surface in the low field side, which can generate a range of RMP spectrum during one discharge for ELM control [127]. The measured intrinsic error field is of the order  $10^{-5}$  (normalized to toroidal field) [117], which provides a good opportunity for RMP ELM control and related 3D physics studies.

ELM suppression with low  $n$  ( $n = 1$  and  $2$ ) RMPs in zero toroidal rotation plasmas with radio-frequency (RF) wave dominant heating and collisionality  $\nu_{e,ped}^* \sim 1$  has been first demonstrated in EAST in 2015 [128]. Evidence of a nonlinear transition from mitigation to suppression of the ELM by using RMPs has been directly observed in the magnetic measurement during the application of  $n=1$  RMPs in EAST [128]. In 2019, full suppression of type-I ELMs using  $n = 4$  RMPs as planned for ITER has been demonstrated for the first time in EAST [129]. The energy confinement drops by a factor of around 20–30% during ELM suppression with a similar amplitude of  $n = 2$  RMPs in a similar target plasma [130].

ELM suppression has also been achieved during the application mixed  $n$  RMPs with  $n = 3$  static and  $n = 2$  rotating fields in DIII-D [131] and EAST [132]. Theoretical modeling has reproduced the linear and nonlinear responses observed on magnetic sensors during ELM mitigation and suppression [133]. The best spectrum for ELM suppression in EAST is consistent with the resonant peak of RMP by taking into account of linear magneto-hydrodynamics plasma response by using the MARS-F code [128, 134]. Clear density pump-out and magnetic braking effects [135] are observed during the application of RMP. A new criterion for controlling edge localized modes based on a multi-mode plasma response is proposed to explain this phase shift [136], and the detailed modeling of plasma response with or without rotation zero crossing has been performed using the MARS-F code [137]. In addition, multimode plasma response has also been directly observed using various methods [138, 139] and agrees well with modeling results. A numerical code TOP2D using field line tracing for modeling of three-dimensional magnetic field topology under RMPs has been developed and validated via comparison to the observed strike point splitting on the divertor using vacuum [140] and plasma response modeling [141] in EAST. Injection of fueling pellets has also been demonstrated for density compensation and stored energy recovery during RMP ELM suppression in EAST [96].

#### 4.2.3 3D physics

To understand ELM suppression physics, a series of studies on 3D physics have also been carried out in EAST. Rotation braking may play an important role in determining RMP field penetration near the edge in low

collisionality regimes. To give a clear physics, we developed the rotation braking modeling (NTVTOK) and carried out Neoclassical toroidal viscosity (NTV) physics studies in many devices [142–152]. Density pump-out is the most common behavior observed in almost all tokamaks during the application of RMP for ELM control in low collisionality regimes. Density pump-out on main ions and impurities [94, 128, 153, 154] and turbulence transport studies [155, 156]. A similar effect on a high-frequency Alfvén-like mode during the inter-ELM phase has also been observed [157]. This mode can also be completely suppressed by RMP before accessing ELM suppression.

In the application of RMP for ELM control in a future fusion reactor, the influences on fast ion confinement and related energetic particle-driven modes have to be considered. The understanding of detailed loss mechanisms may also be helpful to study the control of fast ion profiles in the future. Influence on energetic particle-driven mode has already been observed in EAST recently. An  $n = 2$  TAE mode excited by the application of a static  $n=2$  RMP has been observed for the first time in EAST [158]. We have also carried out lots of simulations on how RMP affects fast ion confinement in EAST. To study the mechanism for fast ion loss during the application of RMPs, various resonant orbit loss effects on trapped particles, such as bounce-drift resonances, recessional resonances, stochastic orbit, have been identified [159]. When plasma response was taken into account, i.e., strong shielding effect on resonant harmonics, it was surprising to find that the loss rate of passing particles with a shielded field with negligible magnetic island width can be even larger than that with vacuum one with big magnetic islands [160]. For better comparison with observations and to study the SOL effect on fast ion loss, a new code SOFT has been developed to simulate the full orbit of particles in real geometry including the SOL area as well [161].

#### 4.2.4 Disruption and runaway electrons

Disruption and their consequences show great challenges during the design and operation processes in tokamak reactors. To further clarify their sensitivities, a series of works have been carried out in EAST. First, Two single deep learning algorithms are trained on a large database of experimental EAST data to classify disruptive discharges and distinguish them from non-disruptive discharges, as shown in Fig. 10 [162–165]. In addition, EAST, together with C-MOD and DIII-D, carried out the cross-device disruption warning research [166–168]. Second, detailed disruption-related studies have been undertaken on EAST [169, 170]. Data from the halo current measurement system [171] shows a significant difference in “W-Like” graphite divertor and “ITER-like” tungsten



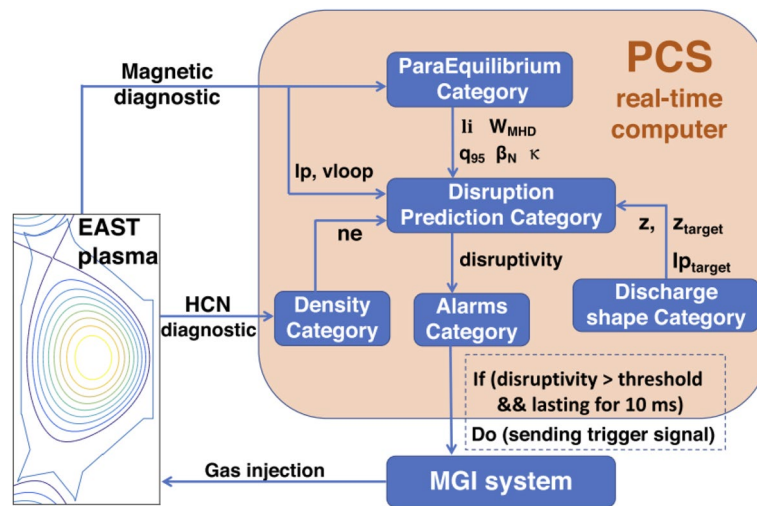


**Fig. 10** The disruption prediction category implemented in the real-time computer of EAST PCS (from Ref [157])

divertor [172]. For W-Like' graphite divertor, most of the halo current flows from the plasma to the copper plate of the divertor. For the ITER-like tungsten divertor, the halo current flows from the outer plate to the inner plate, through the cassette [172]. A massive gas injection valve (MGI) based on the double-layer eddy-current repulsion mechanism has been developed [173] and employed to carry out disruption mitigation [174].

The runaway electron issue is also a great concern in future reactors. The study of runaway electrons during disruptions and analysis of synchrotron radiation emitted by runaway electrons have been carried out in EAST [175–180]. The result during disruptions shows the competition between the radial diffusion of the induced electric field and the growth of the runaway current, and it also indicates that half of the decreasing magnetic energy can be converted into runaway electron kinetic energy during the disruptions [175]. By comparing the synchrotron radiation spectra of runaway electrons based on the full expression, their asymptotic expressions, and pure circular orbit expressions, it is analyzed how radiation spectra and total radiation power of runaway electrons in a tokamak can be analyzed correctly and efficiently [176]. Analysis of synchrotron radiation patterns from runaway electrons indicates that the energy, pitch angle, and  $q$  profile can significantly affect the synchrotron radiation pattern. Particularly, an asymmetrical synchrotron radiation pattern can be deduced when the effect of the drift orbit shift is considered, which can explain the asymmetrical ring-like synchrotron radiation pattern from runaway electron beams in EAST experiments [177, 178]. In the discharge flattop, two different threshold electric fields, characterizing a lower field required for significant seed RE generation and sustainment and a higher field

required for the RE avalanche onset, have been experimentally observed [179]. The threshold electric field for the RE avalanche onset is 1.2-fold higher than the RE detection onset field required for the primary generation. Runaway plateau has also been detected in the unintended disruptions [180]. The highest runaway current corresponds to the lowest loop voltage and this anomalous behavior is attributed to the acceleration of the pre-exciting wave resonant suprathreshold electrons by LHW. Two distinct types of RE-related relaxation phenomena, including kinetic instability driven by medium-energy REs and MHD activity, have been found to cause an amount of RE loss during a runaway plateau.

### 4.3 Pedestal and edge physics

The H-mode operation of EAST was first achieved in the 2010 campaign. The following research suggests that the L-H transition power threshold  $P_{L-H}$  is highly correlated with the edge neutral density, the ion  $\nabla B$  drift, the divertor pumping capability, and the hydrogen concentration [181–183]. A clear 'U-shape' dependence of  $P_{L-H}$  on electron density has been observed in the helium-dominated plasma [90]. Direct probe measurements demonstrate that zonal flows play a role in the slow L-H transition [184], while the shift in radial wave number spectrum of turbulence induced by mean flow shear can mediate the fast L-H transition [185]. Pedestal structure studies indicate that the pedestal width has a strong correlation with the poloidal pedestal beta and could be influenced by the heating schemes and lithium wall coating [55, 186]. The characteristic of the coherent mode in pedestal has been extensively studied [55, 178–195], including the edge coherent mode (ECM) and the magnetic coherent mode (MCM). ECM and  $E \times B$  flow shear are found to facilitate

the achievement of small/no ELM operation at high pedestal collisionality [189, 196, 197]. Massive efforts have been made to develop active ELM control techniques. Reproducible steady-state ELM-free H-mode discharges have been achieved using the real-time injection of lithium (Li) [198] and boron aerosol [199]. Triggering of ELMs has been demonstrated using low-velocity Li granules with nearly 100% efficiency [200]. Sustained ELM suppression has been achieved using CD4 seeding from the divertor region [201]. ELM suppression by ICRF heating has also been observed where the role of  $E \times B$  flow shear induced by the RF sheath has been highlighted [202, 203]. A highly reproducible stationary grassy ELM regime has been achieved [69, 204–206]. The good compatibility of this regime with low torque injection, high plasma density (up to  $\sim 1.1n_{GW}$ ), high bootstrap current fraction ( $f_{BS}$  up to 70%), and radiative divertor has been demonstrated. In addition to the generally considered high  $q_{95}$  and  $\beta_p$ , EAST results indicate that a wide pedestal with a low-density gradient can facilitate the achievement of such small ELMs. This might have a positive implication for future fusion reactors where a low pedestal fueling and a flat pedestal density profile are anticipated [207, 208].

#### 4.4 Divertor and plasma-wall interaction

##### 4.4.1 Wall conditioning and recycling

Controlling of fuel recycling and hydrogen content in deuterium plasma is very important, not only to avoid diluting reacting core deuterons but also the enhancement of plasma performance. During recent years several techniques of surface conditioning such as baking, glow discharge cleaning (GDC), ICRF discharge cleaning, and wall coatings, such as lithium coating, have all been attempted in order to reduce the H/(H+D) ratio and wall recycling in EAST. The necessary clean vacuum environment is provided in EAST by a long first wall baking and discharge cleaning, with a high ultimate vacuum of  $3.6 \times 10^{-6}$  Pa and a low outgassing rate plasma of about  $1.5 \times 10^{-4}$  Pa  $m^3 s^{-1}$  Operation [209]. By using vacuum evaporation and real-time injection of lithium powder to complete the lithium coating, the H/(H + D) ratio can be routinely reduced to approximately 3% [210, 211] and the global recycling coefficient could reduce from 0.94 to 0.82. The in-vessel cryopumps also provide an efficient method for particle recycling control in the divertor region, reducing the global recycling coefficient from  $\sim 1.0$  to  $\sim 0.8$  during ohmic heating of the plasma and provide  $10^{20}$ - $10^{21}$  D atoms exhausting rate [209]. In addition to the lithium coating on EAST, the flowing liquid lithium limiter (FLiLi) can also effectively reduce the particle recycling. Comparing the retention and

recycling with a Li-coated wall, FLiLi could continuously increase fuel particle retention and bring higher fuel particle retention including both short-term and long-term retention as well as lower recycling [212]. Through various wall conditions, the effective control of particle recycling is achieved on EAST, facilitating the acquisition of EAST thousand-second long pulse and more than 300-s H-mode discharges.

##### 4.4.2 Radiating divertor and detachment

The divertor detachment induced by impurity seeding is acknowledged as the most promising means to control the steady-state heat flux and tungsten sputtering for fusion reactors. During detachment, the electron temperature on the divertor target can be reduced to less than 5eV, while the heat load reduction is much more than 50% normally, with the increase of radiative power. In recent years, great efforts and progresses have been made on the radiative divertor physics and active feedback control of detachment with tungsten divertor operation in EAST [66, 213]. The detachment feedback control techniques using divertor Langmuir probe measured divertor particle flux  $j_s$ , electron temperature  $T_{et,div}$  [214],  $T_{et,div}$  guided X-point radiation [69], and IR-camera measured target surface temperature  $T_{t,peak}$  [68] were all successfully developed. Simultaneous double feedback control of core radiation with neon seeding and divertor  $T_{et}$  with Argon seeding from different gas puffing valves for core-edge integration is now under developing. The actively feedback-controlled H-mode detachment at  $T_{et,div} \sim 5$  eV and  $H_{98} > 1$  has been achieved using neon or Ar impurity seeding, with neon being more compatible with sustained good core performance under the present H-mode plasma parameters [214]. The experiments in EAST demonstrate that a closed divertor is beneficial for neutral trapping and thus detachment access [213]. The impurity seeding from around the strike point is much more effective for detachment access and compatible with the core plasma confinement than that with seeding from the upstream scrap-off layer [215]. In the EAST 2021 campaign, the new lower W divertor with a more advanced geometry and active water-cooling capability for the steady-state operation has been successfully upgraded. By employing the new lower W divertor, active detachment feedback control via  $T_{et}$  controller with Argon seeding has been extended to 30 s long-pulse H-mode operation, with active detachment-control duration being 25 s [216]. A slight decrease of the plasma stored energy ( $\sim 8\%$ ) was observed, which was not seen with neon seeding long-pulse H-mode discharge, demonstrating the compatibility of long-pulse detachment and core confinement in EAST.

#### 4.4.3 Tungsten sputtering and erosion control

The upper and lower divertor materials of EAST were upgraded from graphite to tungsten in 2014 and 2021, respectively. After the upgrade of divertor material, a high-time resolution spectroscopy [217] was developed for monitoring the EAST divertor W sputtering, and many dedicated experiments were carried out to investigate the W erosion control. Experimental results reveal that the W erosion rate is strongly related with both the divertor plasma temperature and the impurity concentration. It is experimentally found that the neon (Ne) seeding from the divertor target can increase the W sputtering by increasing the local Ne concentration when the local electron temperature is above 25 eV [218], but the W erosion will be well suppressed after the divertor detachment is achieved [219]. D<sub>2</sub> gas injections from both the outer mid-plane and the divertor target are also proved to be effective ways for W erosion mitigation by reducing the electron temperature on the divertor target [220]. The real-time Li injection technique developed on EAST can change the wall condition during the discharge. Li aerosol dropping from the upper divertor region can cool the edge plasma and make an overlayer on the W surface at the same time, and thus, a significant reduction of W erosion is observed [217, 220]. Intra-ELM W sourcing and temporal evolution are analyzed on EAST. The effective W sputtering during ELMs shows a positive correlation with the pedestal electron temperature and a total W source mitigation is achieved by applying RMP [221]. Due to the migration and deposition of first wall materials, W erosion on the EAST divertor is well reproduced by using mixed material modules [222, 223]. Simulation results indicate that carbon impurity plays an important role on W erosion for both inter- and intra-ELM phases although the energetic D<sup>+</sup> originated from the pedestal region also contributes a nonnegligible part of W erosion during ELMs.

#### 4.5 Energetic particle physics

The energetic particles are mainly driven by NBI and RF heating. On EAST, all the three RF waves (LHW, ECRH, and ICRH) primarily heat the electrons (On EAST the main heating regime of ICRH is the minority heating, it eventually mainly heats the electrons). The fast ions are mainly from the NBI. The ICRH could further accelerate the NBI-driven fast ions, leading to a higher energy tail. This is the so-called synergy effect. This effect was observed on EAST. After the ICRH power was added to the NBI heating plasma, the neutron yield increased and the energy of fast ions was accelerated to larger than 300 keV [Zhang W. et al., Nuclear Fusion, 2022, submitted].

Generally, on EAST RF waves (especially the LHW) dominants the heating power. Therefore, fast

electron-driven modes are widely observed. The first reported fast particle-driven mode was the BAEs excited by LHW [224]. In this study, the strong tearing mode also played an important role: the magnetic reconnection accelerated the electrons and helped to excite the BAEs. Subsequently, double pairs of BAEs (BAE quartet) with the radial discrete structure were observed [225], which can be explained by taking into account physics such as the drift effect and the parallel motion of the ion. The coupling of BAEs, GAMs, and magnetic islands was also investigated [226–228]. It is proposed that the twin BAEs can be excited by the nonlinear interaction between GAM and magnetic islands. Other fast electron excited modes were also observed, such as TAE excited by LHW [229] and by ECRH [230]. Sometimes the low-frequency (20–50 kHz) BAE and high-frequency TAE (120–250 kHz) could be nonlinearly coupled and generate many harmonics (daughter waves).

Typical fast ion-driven modes have been observed on EAST. Figure 11 summarized the existed modes and their parameter range in  $\beta_N - q_{95}$  space. The modes lie in two regions. Actually, the two regions are in the range of the two main scenarios of EAST. The fishbone instability is easily excited for the high  $\beta_N$  scenario with lower  $q_{95}$ , which was firstly observed in the year of 2015 [231]. Later numerical simulation by M3D-K [232] and by MEGA [233] confirms that the fishbone is mainly driven by low energy beam ions via precessional resonance, and the frequency of the fishbone chirps up and down with corresponding hole-clump structures in phase space, consistent with the Berk–Breizman theory [232]. Besides the fishbone mode, the EPM and TAE instabilities [234] are also observed in the high  $\beta_N$  scenario. Interestingly, the establishment of ITBs is often accompanied by the burst of fishbone [235, 236] or RSAE [237, 238] instabilities, and the possible reason is caused by the redistribution of energetic ions. The BAEs [239], RSAEs [240, 241], and EPM instabilities are excited by energetic ions in the high  $\beta_p$  scenario with higher  $q_{95}$ . Similarly, the establishment of ITBs is also accompanied by the excitation of RSAEs (BAEs or AITG-like).

Resonant magnetic perturbations (RMPs) could affect fast particle behavior. It was observed that TAEs were excited in an ohmic heating plasma when the current of a static  $n=2$  RMPs exceeds a threshold value [158]. The behind physics is that the energetic electrons may be accelerated by the magnetic islands, which are formed by the forced magnetic reconnection induced by RMPs. RMPs could also enhance fast ion loss. Numerical simulation on EAST showed that both linear and nonlinear resonances play an important role. And the primary contribution from resonant components and the side-band contribution from non-resonant components are

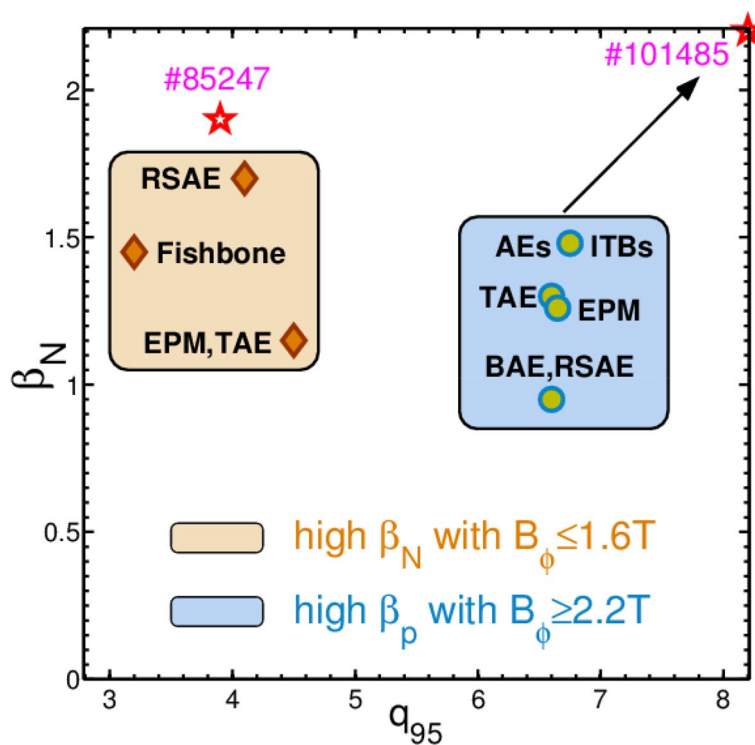


Fig. 11 Parameter range of the fast ion-driven modes existed on EAST

comparable [161]. The experimental study of the fast ion loss induced by RMPs is under investigation.

### 5 Summary

In summary, this paper reviews the machine status and recent research progress on EAST tokamak. Since the start of the project, EAST is making steady progress towards fusion energy research. Continuous upgrades of EAST hardware during the past 16 years, especially the PFC components and H&CD capability strongly supported the scientific mission of EAST.

Aiming at steady-state and high-performance plasma operation, different scenarios have been developed on EAST. Typical results could refer to long-pulse divertor operation (>400s), long-pulse H-mode plasmas with steady-state advanced high  $\beta_p$  regime, development of low  $q_{95}$  H-mode plasmas related to ITER baseline and possible extension to a hybrid scenario, helium H-mode plasma with pure RF power in support of ITER. Various physics studies have been carried out in these scenarios, including transport and confinement, MHD and 3D physics, pedestal and edge physics, divertor and plasma-wall interaction, and energetic particle physics.

In the near future, EAST will continue to develop advanced scenarios for plasma operation, such as

H-mode plasmas in a thousand seconds timescale, to support ITER operation and future fusion reactors, like CFETR.

### Acknowledgements

Contributions to the EAST experiments from domestic and international collaborators (institutions and individuals) are deeply appreciated. This work was supported by the National Key Research and Development Program of China under Contract Nos. (2016YFA0400600, 2017YFA0402500), the National Magnetic Confinement Fusion Science Program of China under Contract Nos. (2019YFE03030000, 2019YFE03040000, 2022YFE03030000, 2022YFE03050000), Major Science and Technology Infrastructure Maintenance and Transformation Project of Chinese Academy of Sciences(DSS-WXGZ-2020-0011, DSS-WXGZ-2021-0009), Performance Improvement Project of EAST, Hefei Comprehensive National Science Center(E05AH10511).

### Authors' contributions

All authors contributed equally to this work. Weibin Xi, Jian Zhang, Liansheng Huang, Damao Yao, Qing Zang, Yanlan Hu, Guizhong Zuo, Qiping Yuan, Zhiwei Zhou, Xinjun Zhang, Mao Wang, Handong Xu, Yahong Xie, Zhengchu Wang, Kun Lu, Junling Chen, Fukun Liu, Jiangang Li, and Yuntao Song contributed to the EAST development and upgrading. Jiasheng Hu, Jinping Qian, Haiqing Liu, Youwen Sun, Liang Wang, Guoqiang Li, Xianzu Gong, and Guosheng Xu contributed to the EAST experiments. Hongxing Yin and Yao Yang contributed to writing the manuscript. All authors review the results and commented on the paper. The authors read and approve the final manuscript.

### Authors' information

All authors belong to the EAST team in the Institute of Plasma Physics, Chinese Academy of Sciences.

### Funding

Not applicable.

**Availability of data and materials**

Supporting information is available from the author or from the reference.

**Declarations****Ethics approval and consent to participate**

Not applicable.

**Consent for publication**

Not applicable.

**Competing interests**

The authors declare that they have no competing interests.

Received: 30 December 2022 Accepted: 23 March 2023

Published online: 11 April 2023

**References**

1. Y.T. Song et al., in *21th International Atomic Energy Agency Fusion Energy Conference in Cheng Du, China 16-21 Oct.* Design, fabrication and testing results of vacuum vessel, thermal shield and cryostat of EAST (2006)
2. B.N. Wan et al., *Sci Sin-Phys Mech. Astron.* **49**, 045205 (2019). <https://doi.org/10.1360/SSPMA2018-00233>
3. P.D. Weng et al., in *21th International Atomic Energy Agency Fusion Energy conference in Cheng Du, China 16-21 Oct.* The engineering commissioning of EAST superconducting tokamak (2006)
4. Wan YX. et al *HT-7U* superconducting Tokamak: physics design, engineering progress and schedule 19th IAEA Fusion Energy Conference proceeding 368
5. J.G. Li, The status and progress of tokamak research. *Physics* **45**, 88 (2016). <https://doi.org/10.7693/wl20160203>
6. J. Wei et al., *IEEE Trans. Appl. Superconductivity* **20**, 556 (2010). <https://doi.org/10.1109/TASC.2010.2040030>
7. S.T. Wu et al., *Fusion Eng. Des.* **73**, 135 (2005). <https://doi.org/10.1016/j.fusengdes.2005.04.002>
8. J. Jiang et al., *Diangong Jishu Xuebao/Trans. China Electrotechnical Soc.* **22**, 118 (2007). <https://doi.org/10.19595/j.cnki.1000-6753.tces.2007.09.021>
9. J. Jiang et al., *High voltage Eng.* **35**, 186 (2009). <https://doi.org/10.13336/j.1003-6520.hve.2009.01.010>
10. P. Fu et al., *Trans. China Electro Tech. Soc.* **19**, 34 (2004). <https://doi.org/10.19595/j.cnki.1000-6753.tces.2004.08.005>
11. P. Fu et al., *Fusion Sci. Technol.* **54**, 1003 (2008). <https://doi.org/10.13182/FST08-A1916>
12. Z. Song et al., *High Voltage Apparatus* **41**, 245 (2005). <https://doi.org/10.13296/j.1001-1609.hva.2005.04.002>
13. D. Li et al., *Diangong Jishu Xuebao/Trans. China Electrotechnical Soc.* **21**, 99 (2006). <https://doi.org/10.19595/j.cnki.1000-6753.tces.2006.09.017>
14. B.N. Wan et al., *SCIENTIA SINICA Physica. Mech. Astronom.* **49**, 045205 (2019). <https://doi.org/10.1360/SSPMA2018-00233>
15. B.N. Wan et al., *Magnet. Fusion Energy.* **60**, 409 (2016). <https://doi.org/10.1016/B978-0-08-100315-2.00013-1>
16. J.S. Hu et al., *Fusion Eng. Des.* **84**, 2167 (2009). <https://doi.org/10.1016/j.fusengdes.2009.03.016>
17. Y. Chen et al., *Physics Procedia* **32**, 14 (2012). <https://doi.org/10.1016/j.phpro.2012.03.512>
18. H.Y. Wang et al., *Physics Procedia* **32**, 235 (2012). <https://doi.org/10.1016/j.phpro.2012.03.548>
19. H.Y. Bai et al., *Fusion Eng. Des.* **81**, 2597 (2006). <https://doi.org/10.1016/j.fusengdes.2006.07.048>
20. L.L. Qiu et al., *Fusion Eng. Des.* **86**, 2821 (2011). <https://doi.org/10.1016/j.fusengdes.2011.05.002>
21. Z.W. Zhou et al., *IOP Conf. Ser.: Mater. Sci. Eng.* **278**, 012120 (2017). <https://doi.org/10.1088/1757-899X/278/1/012120>
22. Z.W. Zhou et al., *IOP Conf. Ser.: Mater. Sci. Eng.* **1240**, 012070 (2022). <https://doi.org/10.1088/1757-899X/1240/1/012070>
23. J.G. Li et al., *2014 Phys. Scr.* **2014**, 014001 (2014). <https://doi.org/10.1088/0031-8949/2014/T1159/014001>
24. L. Cao et al., *J. Fusion Energ.* **34**, 1451 (2015). <https://doi.org/10.1007/s10894-015-9951-2>
25. Z.B. Zhou et al., *J. Fusion Energ.* **34**, 93 (2015). <https://doi.org/10.1007/s10894-014-9765-7>
26. G.N. Luo et al., *Nucl. Fusion* **57**, 065001 (2017). <https://doi.org/10.1088/1741-4326/aa6502>
27. Y.T. Song et al., *Fusion Eng. Des.* **85**, 2323 (2010). <https://doi.org/10.1016/j.fusengdes.2010.09.020>
28. J.P. Qian et al., *Plasma Sci. Technol.* **13**, 1 (2011). <https://doi.org/10.1088/1009-0630/13/1/01>
29. B.F. Gao et al., *Fusion Eng. Des.* **156**, 111616 (2020). <https://doi.org/10.1016/j.fusengdes.2020.111616>
30. L. Wang et al., *J. Fusion Energ.* **40**, 3 (2021). <https://doi.org/10.1007/s10894-021-00290-9>
31. Q. Zhuang et al., *Fusion Eng. Des.* **179**, 113137 (2022). <https://doi.org/10.1016/j.fusengdes.2022.113137>
32. G.S. Xu et al., *Nucl. Fusion* **61**, 126070 (2021). <https://doi.org/10.1088/1741-4326/ac3297>
33. J.F. Shan, in *Proceedings of the 23rd IAEA Fusion Energy Conference, Daejeon, Korea.* A new 4 MW LHCD system for EAST (2010) [https://www-pub.iaea.org/MTCD/Meetings/PDFplus/2010/cn180/cn180\\_papers/exw\\_p7-29.pdf](https://www-pub.iaea.org/MTCD/Meetings/PDFplus/2010/cn180/cn180_papers/exw_p7-29.pdf)
34. F.K. Liu et al., *Fusion Eng. Des.* **113**, 131 (2016). <https://doi.org/10.1016/j.fusengdes.2016.10.020>
35. L.M. Zhao et al., *Plasma Sci. Technol.* **12**, 118 (2011). <https://doi.org/10.1088/1009-0630/12/1/25>
36. M.H. Li et al., *Fusion Eng. Des.* **147**, 111250 (2019). <https://doi.org/10.1016/j.fusengdes.2019.111250>
37. M. Wang et al., *Nucl. Eng. Technol.* **54**, 4102 (2022). <https://doi.org/10.1016/j.net.2022.06.003>
38. W.D. Ma et al., *Rev. Sci. Instrum.* **90**, 113506 (2019). <https://doi.org/10.1063/1.5117177>
39. M. Wang et al., *IEEE ACCESS* **6**, 37413 (2018). <https://doi.org/10.1109/ACCESS.2018.2851982>
40. Y.P. Zhao et al., *Fusion Eng. Des.* **89**, 2642 (2014). <https://doi.org/10.1016/j.fusengdes.2014.06.017>
41. X.J. Zhang et al., *Plasma Sci. Technol.* **13**, 172 (2011). <https://doi.org/10.1088/1009-0630/13/2/09>
42. X.J. Zhang et al., *Nucl. Fusion* **52**, 032002 (2012). <https://doi.org/10.1088/0029-5515/52/3/032002>
43. X.J. Zhang et al., *Nucl. Fusion* **53**, 023004 (2013). <https://doi.org/10.1088/0029-5515/53/2/023004>
44. X.J. Zhang et al., *Nucl. Fusion* **62**, 086038 (2022). <https://doi.org/10.1088/1741-4326/ac7657>
45. H. Xu et al., *Plasma Sci. Technol.* **18**, 442 (2016). <https://doi.org/10.1088/1009-0630/18/4/19>
46. H. Xu et al., *Fusion Eng. Des.* **164**, 112222 (2021). <https://doi.org/10.1016/j.fusengdes.2020.112222>
47. C. Hu et al., *Plasma Sci. Technol.* **17**, 817 (2015). <https://doi.org/10.1088/1009-0630/17/10/02>
48. B. Wu et al., *Fusion Eng. Des.* **86**, 947 (2011). <https://doi.org/10.1016/j.fusengdes.2011.01.148>
49. C.D. Hu et al., *Plasma Sci. Technol.* **17**, 1 (2015). <https://doi.org/10.1088/1009-0630/17/1/01>
50. Y.H. Xie et al., *IEEE Trans. Plasma Sci.* **1** (2022). <https://doi.org/10.1109/TPS.2022.3164682>
51. C.C. Jiang et al., *Rev. Sci. Instrum.* **86**, 056110 (2015). <https://doi.org/10.1063/1.4921705>
52. Y.H. Xie et al., *Plasma Sci. Technol.* **21**, 105601 (2019). <https://doi.org/10.1088/2058-6272/ab2a8e>
53. B.N. Wan et al., *Nucl. Fusion* **59**, 112003 (2019). <https://doi.org/10.1088/1741-4326/ab0396>
54. Q. Zang et al., *Rev. Sci. Instrum.* **82**, 063502 (2011). <https://doi.org/10.1063/1.3599039>
55. Q. Zang et al., *Nucl. Fusion* **56**, 106003 (2016). <https://doi.org/10.1088/0029-5515/56/10/106003>
56. Y. Shi et al., *Plasma Phys. Control. Fusion* **52**, 085014 (2010). <https://doi.org/10.1088/0741-3335/52/8/085014>
57. J. Su et al., *Plasma Sci. Technol.* **23**, 095103 (2021). <https://doi.org/10.1088/2058-6272/ac0cce>

58. Y. Wang et al., *Fusion Eng. Des.* **144**, 133 (2019). <https://doi.org/10.1016/j.fusengdes.2019.05.002>
59. Y. Huang et al., *Fusion Eng. Des.* **120**, 1 (2017). <https://doi.org/10.1016/j.fusengdes.2017.05.005>
60. Z. Zhang et al., *Fusion Eng. Des.* **89**, 582 (2014). <https://doi.org/10.1016/j.fusengdes.2014.03.030>
61. Y. Chen et al., *IEEE Trans. Nucl. Sci.* **66**, 1304 (2019). <https://doi.org/10.1109/TNS.2019.2903792>
62. F. Wang et al., *Fusion Eng. Des.* **129**, 88 (2018). <https://doi.org/10.1016/j.fusengdes.2018.02.068>
63. Y. Chen et al., *Fusion Eng. Des.* **129**, 83 (2018). <https://doi.org/10.1016/j.fusengdes.2018.02.080>
64. B. Xiao et al., *Fusion Eng. Des.* **83**, 181 (2008). <https://doi.org/10.1016/j.fusengdes.2007.12.028>
65. Q. Yuan et al., *Nucl. Fusion* **53**, 043009 (2013). <https://doi.org/10.1088/0029-5515/53/4/043009>
66. K. Wu et al., *Nucl. Fusion* **58**, 056019 (2018). <https://doi.org/10.1088/1741-4326/aab506>
67. Q. Yuan et al., *Fusion Eng. Des.* **154**, 111557 (2020). <https://doi.org/10.1016/j.fusengdes.2020.11.1557>
68. M. Chen et al., *Nucl. Fusion* **60**, 076009 (2020). <https://doi.org/10.1088/1741-4326/ab8c65>
69. G. Xu et al., *Nucl. Fusion* **60**, 086001 (2020). <https://doi.org/10.1088/1741-4326/ab91fa>
70. Y. Wang et al., *Fusion Eng. Des.* **112**, 692 (2016). <https://doi.org/10.1016/j.fusengdes.2016.05.008>
71. Y. Guo et al., *Nucl. Fusion* **60**, 076002 (2020). <https://doi.org/10.1088/1741-4326/ab8775>
72. R. Albanese et al., *Nucl. Fusion* **57**, 086039 (2017). <https://doi.org/10.1088/1741-4326/aa7a78>
73. Y. Huang et al., *Nucl. Fusion* **60**, 076023 (2020). <https://doi.org/10.1088/1741-4326/ab91f8>
74. X. Yue et al., *Plasma Physics Controlled Fusion* **55**, 8 (2013). <https://doi.org/10.1088/0741-3335/55/8/085016>
75. Y. Huang et al., *Chin. Physics B* **08**, 280 (2017). <https://doi.org/10.1088/1674-1056/26/8/085204>
76. Y. Huang et al., *Fusion Eng. Des.* **128**, 82 (2018). <https://doi.org/10.1016/j.fusengdes.2018.01.043>
77. Y. Wang et al., *Fusion Eng. Des.* **142**, 1 (2019). <https://doi.org/10.1016/j.fusengdes.2019.04.067>
78. Q. Yuan et al., *IEEE Trans. Plasma Sci.* **46**, 1356 (2018). <https://doi.org/10.1109/TPS.2018.2805784>
79. B. Wan et al., *Nucl. Fusion* **53**, 104006 (2013). <https://doi.org/10.1088/0029-5515/53/10/104006>
80. X.Z. Gong et al., *Plasma Sci. Tech.* **25**, 022001 (2023). <https://doi.org/10.1088/2058-6272/ac9cc6>
81. E.Z. Li et al., *Phys. Rev. Lett.* **128**, 085003 (2022). <https://doi.org/10.1103/PhysRevLett.128.085003>
82. J.W. Liu et al., *Nucl. Fusion* **63**, 016011 (2023). <https://doi.org/10.1088/1741-4326/aca168>
83. Y.T. Song et al., *Sci. Adv.* **9**, eabq5273 (2023). <https://doi.org/10.1126/sciadv.abq5273>
84. B. Wan et al., *Nucl. Fusion* **55**, 104015 (2015). <https://doi.org/10.1088/0029-5515/55/10/104015>
85. A.M. Garofalo et al., *Nucl. Fusion* **57**, 076037 (2017). <https://doi.org/10.1088/1741-4326/aa7186>
86. X. Gong et al., *Nucl. Fusion* **59**, 086030 (2019). <https://doi.org/10.1088/1741-4326/ab1c7b>
87. J.P. Qian et al., *Phys. Plasmas* **28**, 042506 (2021). <https://doi.org/10.1063/5.0032490>
88. G. Zhuang et al., *Nucl. Fusion* **59**, 112010 (2019). <https://doi.org/10.1088/1741-4326/ab0e27>
89. X. Gao et al., *Nucl. Fusion* **60**, 102001 (2020). <https://doi.org/10.1088/1741-4326/abaa91>
90. B. Zhang et al., *Nucl. Fusion* **60**, 092001 (2020). <https://doi.org/10.1088/1741-4326/ab9be6>
91. Y. Liu et al., *Nucl. Fusion* **59**, 044005 (2019). <https://doi.org/10.1088/1741-4326/ab0665>
92. Y. Liu et al., *Nucl. Fusion* **59**, 106024 (2019). <https://doi.org/10.1088/1741-4326/ab3541>
93. S.X. Wang et al., *Phys. Plasmas* **26**, 052515 (2019). <https://doi.org/10.1063/1.5088979>
94. S.X. Wang et al., *Nucl. Fusion* **58**, 112013 (2018). <https://doi.org/10.1088/1741-4326/aae15a>
95. J.L. Hou et al., *Plasma Phys. Control. Fusion* **64**, 055010 (2022). <https://doi.org/10.1088/1361-6587/ac6048>
96. J.L. Hou et al., *Nucl. Fusion* **59**, 096039 (2019). <https://doi.org/10.1088/1741-4326/ab2bd3>
97. B. Lyu et al., *Rev. Sci. Instrum.* **89**, 10F112 (2018). <https://doi.org/10.1063/1.5039314>
98. Y.J. Shi et al., *Phys. Rev. Lett.* **106**, 235001 (2011). <https://doi.org/10.1103/PhysRevLett.106.235001>
99. X.Y. Pan et al., *Plasma Sci. Technol.* **18**, 114 (2016). <https://doi.org/10.1088/1009-0630/18/2/03>
100. Y.F. Jin et al., *Plasma Phys. Control. Fusion* **64**, 095012 (2022). <https://doi.org/10.1088/1361-6587/ac828e>
101. L. Zhang et al., *Rev. Sci. Instrum.* **86**, 123509 (2015). <https://doi.org/10.1063/1.4937723>
102. L. Zhang et al., *Nuclear Inst. Methods Physics Res. A* **916**, 169–178 (2019). <https://doi.org/10.1016/j.nima.2018.11.082>
103. Y. Cheng et al., *Rev. Sci. Instrum.* **93**, 123501 (2022). <https://doi.org/10.1063/5.0104225>
104. Z. Xu et al., *Nucl. Fusion* **58**, 016001 (2018). <https://doi.org/10.1088/1741-4326/aa8e06>
105. Z. Xu et al., *Chin. Phys. B* **30**, 075205 (2021). <https://doi.org/10.1088/1674-1056/abe1a6>
106. W. Xu et al., *Plasma Phys. Control. Fusion* **62**, 085012 (2020). <https://doi.org/10.1088/1361-6587/ab9b3a>
107. S.Y. Shi et al., *Nucl. Fusion* **62**, 066032 (2022). <https://doi.org/10.1088/1741-4326/ac3e3b>
108. S.Y. Shi et al., *Nucl. Fusion* **62**, 066031 (2022). <https://doi.org/10.1088/1741-4326/ac3e3c>
109. L. Xu et al., *Plasma Phys. Control. Fusion* **55**, 032001 (2013). <https://doi.org/10.1088/0741-3335/55/3/032001>
110. L. Xu et al., *Phys. Plasmas* **19**, 122504 (2012). <https://doi.org/10.1063/1.4773032>
111. Y. Yuan et al., *Nucl. Fusion* **60**, 016003 (2019). <https://doi.org/10.1088/1741-4326/ab455b>
112. L. Xu et al., *Nucl. Fusion* **60**, 106027 (2020). <https://doi.org/10.1088/1741-4326/abadab>
113. Y. Yuan et al., *Phys. Plasmas* **23**, 062503 (2016). <https://doi.org/10.1063/1.4953605>
114. Y. Zhang et al., *Fusion Sci. Technol.* **70**, 62–72 (2016). <https://doi.org/10.13182/FST15-138>
115. X.G. Wang et al., *Phys. Plasmas* **22**, 022512 (2015). <https://doi.org/10.1063/1.4913352>
116. Y. Zhang et al., *Nucl. Fusion* **61**, 096028 (2021). <https://doi.org/10.1088/1741-4326/ac0bfb>
117. X.J. Wang et al., *Plasma Phys. Control. Fusion* **60**, 045004 (2018). <https://doi.org/10.1088/1361-6587/aaa864>
118. X.J. Wang et al., *Nucl. Fusion* **58**, 016045 (2018). <https://doi.org/10.1088/1741-4326/aa944e>
119. X.J. Wang et al., *Nucl. Fusion* **62**, 066007 (2022). <https://doi.org/10.1088/1741-4326/ac55b9>
120. X.G. Wang et al., *Nucl. Fusion* **55**, 093024 (2015). <https://doi.org/10.1088/0029-5515/55/9/093024>
121. H.H. Wang et al., *Nucl. Fusion* **56**, 066011 (2016). <https://doi.org/10.1088/0029-5515/56/6/066011>
122. H.H. Wang et al., *Nucl. Fusion* **58**, 056024 (2018). <https://doi.org/10.1088/1741-4326/aab5c0>
123. C. Ye et al., *Nucl. Fusion* **61**, 056010 (2021). <https://doi.org/10.1088/1741-4326/abed5>
124. H.H. Wang et al., *Nucl. Fusion* **60**, 126008 (2020). <https://doi.org/10.1088/1741-4326/abaff7>
125. J. Ren et al., *Nucl. Fusion* **61**, 056007 (2021). <https://doi.org/10.1088/1741-4326/abea57>
126. Y. Sun et al., *Plasma Phys. Control. Fusion* **57**, 045003 (2015). <https://doi.org/10.1088/0741-3335/57/4/045003>
127. Y. Sun et al., *Nucl. Fusion* **57**, 036007 (2017). <https://doi.org/10.1088/1741-4326/57/3/036007>

128. Y. Sun et al., *Phys. Rev. Lett.* **117**, 115001 (2016). <https://doi.org/10.1103/PhysRevLett.117.115001>
129. Y. Sun et al., *Nucl. Fusion* **61**, 106037 (2021). <https://doi.org/10.1088/1741-4326/ac1a1d>
130. M. Jia et al., *Nucl. Fusion* **61**, 106023 (2021). <https://doi.org/10.1088/1741-4326/ac21f9>
131. M. Jia et al., *Physics Plasmas* **25**, 056102 (2018). <https://doi.org/10.1063/1.5019777>
132. Sun Y. et al 2018 IAEA Fusion Energy Conf. (Gandhinagar, India 22–27 October 2018) pp EX/7–2 ‘Dynamic ELM and divertor control using mixed toroidal harmonic resonant magnetic perturbations in DIII-D and EAST’, (<https://conferences.iaea.org/event/151/contributions/6358/>)
133. S. Gu et al., *Nucl. Fusion* **59**, 026012 (2019). <https://doi.org/10.1088/1741-4326/aaf5a3>
134. X. Yang et al., *Plasma Phys. Control. Fusion* **58**, 114006 (2016). <https://doi.org/10.1088/0741-3335/58/11/114006>
135. X.Y. Li et al., *Phys. Plasmas* **26**, 052512 (2019). <https://doi.org/10.1063/1.5098526>
136. S. Gu et al., *Nucl. Fusion* **59**, 126042 (2019). <https://doi.org/10.1088/1741-4326/ab4566>
137. P. Xie et al., *Phys. Plasmas* **28**, 092511 (2021). <https://doi.org/10.1063/5.0062540>
138. N. Logan et al., *Nucl. Fusion* **58**, 076016 (2018). <https://doi.org/10.1088/1741-4326/aac129>
139. Z.R. Wang et al., *Nucl. Fusion* **59**, 024001 (2019). <https://doi.org/10.1088/1741-4326/aaf671>
140. M. Jia et al., *Plasma Phys. Control. Fusion* **58**, 055010 (2016). <https://doi.org/10.1088/0741-3335/58/5/055010>
141. M. Jia et al., *Nucl. Fusion* **58**, 046015 (2018). <https://doi.org/10.1088/1741-4326/aaaec3>
142. Y. Sun et al., *Phys. Rev. Lett.* **105**, 145002 (2010). <https://doi.org/10.1103/PhysRevLett.105.145002>
143. Y. Sun et al., *Nucl. Fusion* **53**, 073026 (2013). <https://doi.org/10.1088/0029-5515/53/7/073026>
144. Y. Sun et al., *Nucl. Fusion* **51**, 053015 (2011). <https://doi.org/10.1088/0029-5515/51/5/053015>
145. Y. Sun et al., *Phys. Plasmas* **26**, 072504 (2019). <https://doi.org/10.1063/1.5099376>
146. Y. Liu et al., *Phys. Plasmas* **20**, 042503 (2013). <https://doi.org/10.1063/1.4799535>
147. Y. Sun et al., *Plasma Phys. Controlled Fusion* **52**, 105007 (2010). <https://doi.org/10.1088/0741-3335/52/10/105007>
148. Y. Sun et al., *Nucl. Fusion* **52**, 083007 (2012). <https://doi.org/10.1088/0029-5515/52/8/083007>
149. L. Frassinetti et al., *Nucl. Fusion* **55**, 112003 (2015). <https://doi.org/10.1088/0029-5515/55/11/112003>
150. Y. Sun et al., *Nucl. Fusion* **53**, 093010 (2013). <https://doi.org/10.1088/0029-5515/53/9/093010>
151. X. Yan et al., *Phys. Plasmas* **28**, 112502 (2021). <https://doi.org/10.1063/5.0056610>
152. H. Li et al., *Nucl. Fusion* **61**, 104002 (2021). <https://doi.org/10.1088/1741-4326/ac1ab0>
153. G. Vogel et al., *J. Plasma Phys.* **87**, 905870213 (2021). <https://doi.org/10.1017/S0022377821000222>
154. S.C. Liu et al., *Nucl. Fusion* **60**, 082001 (2020). <https://doi.org/10.1088/1741-4326/ab77e5>
155. T. Zhang et al., *Phys. Plasmas* **26**, 092504 (2019). <https://doi.org/10.1063/1.5119020>
156. G.H. Hu et al., *Nucl. Fusion* **60**, 016020 (2020). <https://doi.org/10.1088/1741-4326/ab4ebf>
157. J.Q. Zhao et al., *Plasma Sci. Technol.* **23**(9), 095101 (2021). <https://doi.org/10.1088/2058-6272/ac06b8>
158. N. Chu et al., *Nucl. Fusion* **58**, 104004 (2018). <https://doi.org/10.1088/1741-4326/aad70c>
159. K. He et al., *Nucl. Fusion* **59**, 126026 (2019). <https://doi.org/10.1088/1741-4326/ab3f80>
160. K. He et al., *Nucl. Fusion* **60**, 126027 (2020). <https://doi.org/10.1088/1741-4326/abb422>
161. K. He et al., *Nucl. Fusion* **61**, 016009 (2021). <https://doi.org/10.1088/1741-4326/abbe74>
162. B.H. Guo et al., *Plasma Phys. Control. Fusion* **63**, 025008 (2020). <https://doi.org/10.1088/1361-6587/abcbbab>
163. B.H. Guo et al., *Plasma Phys. Control. Fusion* **63**, 115007 (2021). <https://doi.org/10.1088/1361-6587/ac228b>
164. K. Zhang et al., *Plasma Sci. Technol.* **22**, 115602 (2020). <https://doi.org/10.1088/2058-6272/abb28f>
165. W.H. Hu et al., *Nucl. Fusion* **61**, 066034 (2021). <https://doi.org/10.1088/1741-4326/abf74d>
166. K.J. Montes et al., *Nucl. Fusion* **59**, 096015 (2019). <https://doi.org/10.1088/1741-4326/ab1df4>
167. J.X. Zhu et al., *Nucl. Fusion* **61**, 049501 (2021). <https://doi.org/10.1088/1741-4326/abe2e3>
168. J.X. Zhu et al., *Nucl. Fusion* **61**, 114005 (2021). <https://doi.org/10.1088/1741-4326/ac28ae>
169. D. Chen et al., *Chin. Phys. B* **24**, 025205 (2015). <https://doi.org/10.1088/1674-1056/24/2/025205>
170. T. Tang et al., *J. Plasma Phys.* **86**, 905860509 (2020). <https://doi.org/10.1017/S0022377820000896>
171. D.L. Chen et al., *Rev. Sci. Instrum.* **86**, 103506 (2015). <https://doi.org/10.1063/1.4932545>
172. D.L. Chen et al., *Plasma Phys. Control. Fusion* **62**, 095019 (2020). <https://doi.org/10.1088/1361-6587/aba366>
173. H.D. Zhuang et al., *Rev. Sci. Instrum.* **86**, 053502 (2015). <https://doi.org/10.1063/1.4920999>
174. D.L. Chen et al., *Nucl. Fusion* **58**, 036003 (2018). <https://doi.org/10.1088/1741-4326/aaa139>
175. R.J. Zhou et al., *Nucl. Fusion* **57**, 114002 (2017). <https://doi.org/10.1088/1741-4326/aa7c9d>
176. M. Xiao et al., *Phys. Plasmas* **24**, 124504 (2017). <https://doi.org/10.1063/1.5009772>
177. R.J. Zhou et al., *Phys. Plasmas* **21**, 063302 (2014). <https://doi.org/10.1063/1.4881469>
178. R.J. Zhou et al., *Plasma Phys. Control. Fusion* **55**, 055006 (2013). <https://doi.org/10.1088/0741-3335/55/5/055006>
179. X. bZhu et al., *Nucl. Fusion* **60**, 084002 (2020). <https://doi.org/10.1088/1741-4326/ab96f3>
180. T. Tang et al., *Nucl. Fusion* **61**, 076003 (2021). <https://doi.org/10.1088/1741-4326/abf62f>
181. G. Xu et al., *Nucl. Fusion* **51**, 072001 (2011). <https://doi.org/10.1088/0029-5515/51/7/072001>
182. L. Chen et al., *Nucl. Fusion* **56**, 056013 (2016). <https://doi.org/10.1088/0029-5515/56/5/056013>
183. L. Shao et al., *Nucl. Fusion* **61**, 016010 (2021). <https://doi.org/10.1088/1741-4326/abfb34>
184. G. Xu et al., *Phys. Rev. Lett.* **107**, 125001 (2011). <https://doi.org/10.1103/PhysRevLett.107.125001>
185. G. Xu et al., *Phys. Rev. Lett.* **116**, 095002 (2016). <https://doi.org/10.1103/PhysRevLett.116.095002>
186. K. Li et al., *Plasma Phys. Control. Fusion* **62**, 115007 (2020). <https://doi.org/10.1088/1361-6587/abb522>
187. H. Wang et al., *Phys. Rev. Lett.* **112**, 185004 (2014). <https://doi.org/10.1103/PhysRevLett.112.185004>
188. X. Gao et al., *Nucl. Fusion* **55**, 083015 (2015). <https://doi.org/10.1088/0029-5515/55/8/083015>
189. Y. Ye et al., *Nucl. Fusion* **57**, 086041 (2017). <https://doi.org/10.1088/1741-4326/aa7809>
190. F. Zhong et al., *Nucl. Fusion* **58**, 056014 (2018). <https://doi.org/10.1088/1741-4326/aab30a>
191. R. Chen et al., *Nucl. Fusion* **58**, 112004 (2018). <https://doi.org/10.1088/1741-4326/aab96e>
192. T. Zhang et al., *Nucl. Fusion* **59**, 056020 (2019). <https://doi.org/10.1088/1741-4326/ab0755>
193. H. Lan et al., *Phys. Plasmas* **26**, 122505 (2019). <https://doi.org/10.1063/1.5123734>
194. N. Zhao et al., *Nucl. Fusion* **61**, 046013 (2021). <https://doi.org/10.1088/1741-4326/abd7b9>
195. Y. Ye et al., *Nucl. Fusion* **61**, 126050 (2021). <https://doi.org/10.1088/1741-4326/ac33c7>
196. D. Kong et al., *Nucl. Fusion* **59**, 016016 (2019). <https://doi.org/10.1088/1741-4326/aaef0c>

197. K. Geng et al., *Nucl. Fusion* **61**, 056011 (2021). <https://doi.org/10.1088/1741-4326/abe08e>
198. J. Hu et al., *Phys. Rev. Lett.* **114**, 055001 (2015). <https://doi.org/10.1103/PhysRevLett.114.055001>
199. Z. Sun et al., *Nucl. Fusion* **61**, 014002 (2021). <https://doi.org/10.1088/1741-4326/abc763>
200. D.K. Mansfield, *Nucl. Fusion* **53**, 113023 (2013). <https://doi.org/10.1088/0029-5515/53/11/113023>
201. Y. Ye, *Nucl. Fusion* **61**, 116032 (2021). <https://doi.org/10.1088/1741-4326/ac26eb>
202. X. Zhang et al., *Sci. China-Phys. Mech. Astron.* **65**, 235211 (2022). <https://doi.org/10.1007/s11433-021-1817-8>
203. Y. Li et al., *Nucl. Fusion* **62**, 066043 (2022). <https://doi.org/10.1088/1741-4326/ac4efd>
204. G. Xu et al., *Phys. Rev. Lett.* **122**, 255001 (2019). <https://doi.org/10.1103/PhysRevLett.122.255001>
205. Q. Yang et al., *Nucl. Fusion* **60**, 076012 (2020). <https://doi.org/10.1088/1741-4326/ab8e0f>
206. G. Ding et al., *Plasma Sci. Technol.* **23**, 095105 (2021). <https://doi.org/10.1088/2058-6272/ac061b>
207. M. Romanelli, *Nucl. Fusion* **55**, 093008 (2015). <https://doi.org/10.1088/0029-5515/55/9/093008>
208. Y. Wang et al., *Nucl. Fusion* **61**, 016032 (2021). <https://doi.org/10.1088/1741-4326/abc59b>
209. Y.W. Yu et al., *Nucl. Fusion* **59**, 126036 (2019). <https://doi.org/10.1088/1741-4326/ab3ead>
210. G.Z. Zuo et al., *Fusion Eng. Design* **131**, 41 (2018). <https://doi.org/10.1016/j.fusengdes.2018.03.065>
211. G.Z. Zuo et al., *Plasma Phys. Control. Fusion* **54**, 015014 (2011). <https://doi.org/10.1088/0741-3335/54/1/015014>
212. C.L. Li et al., *Plasma Phys. Control. Fusion* **63**, 015001 (2020). <https://doi.org/10.1088/1361-6587/abc396>
213. L. Wang et al., *Nucl. Fusion* **22**, 076002 (2022). <https://doi.org/10.1088/1741-4326/ac4774>
214. D. Eldon et al., *Nucl. Mater. Energy* **27**, 100963 (2021). <https://doi.org/10.1016/j.nme.2021.100963>
215. K.D. Li et al., *Nucl. Fusion* **61**, 066013 (2021). <https://doi.org/10.1088/1741-4326/abf418>
216. L.Y. Meng et al., *Nucl. Fusion* **22**, 086027 (2022). <https://doi.org/10.1088/1741-4326/ac74cf>
217. H. Mao et al., *Nucl. Mater. Energy* **12**, 447–452 (2017). <https://doi.org/10.1016/j.nme.2016.12.010>
218. D. Ye et al., *Chin. Phys. B* **31**, 065201 (2022). <https://doi.org/10.1088/1674-1056/ac4f58>
219. R. Ding et al., *Nucl. Mater. Energy* **101250** (2022). <https://doi.org/10.1016/j.nme.2022.101250>
220. F. Ding et al., *Tungsten* **1**, 122–131 (2019). <https://doi.org/10.1007/s42864-019-00019-4>
221. X. Chen et al., *Nucl. Fusion* **61**, 46046 (2021). <https://doi.org/10.1088/1741-4326/abe697>
222. H. Xie et al., *Phys. Plasmas* **24**, 92512 (2017). <https://doi.org/10.1063/1.4991457>
223. G. Xu et al., *Nucl. Fusion* **61**, 86011 (2021). <https://doi.org/10.1088/1741-4326/ac086a>
224. M. Xu et al., *Plasma Physics Controlled Fusion* **55**, 065002 (2013). <https://doi.org/10.1088/0741-3335/55/6/065002>
225. M. Xu et al., *Nucl. Fusion* **58**, 124004 (2018). <https://doi.org/10.1088/1741-4326/aae8b7>
226. M. Xu et al., *Nucl. Fusion* **58**, 096004 (2018). <https://doi.org/10.1088/1741-4326/aac8a3>
227. M. Xu et al., *Nucl. Fusion* **61**, 036034 (2021). <https://doi.org/10.1088/1741-4326/abd72d>
228. H. Qu et al., *Plasma Physics Controlled Fusion* **64**, 054007 (2022). <https://doi.org/10.1088/1361-6587/ac5a0c>
229. W. Hu et al., *Nucl. Fusion* **58**, 096032 (2018). <https://doi.org/10.1088/1741-4326/aacfad>
230. N. Chu et al., *Nucl. Fusion* **61**, 046021 (2021). <https://doi.org/10.1088/1741-4326/abe4b1>
231. L. Xu et al., *Physics Plasmas* **22**, 122510 (2015). <https://doi.org/10.1063/1.4939020>
232. W. Shen et al., *Nucl. Fusion* **57**, 116035 (2017). <https://doi.org/10.1088/1741-4326/aa7f9c>
233. Y. Pei et al., *Physics Plasmas* **24**, 032507 (2017). <https://doi.org/10.1063/1.4978562>
234. L. Xu et al., *Nucl. Fusion* **61**, 076005 (2021). <https://doi.org/10.1088/1741-4326/abf2e2>
235. X. Gao, *Physics Lett. A* **382**, 1242 (2018). <https://doi.org/10.1016/j.physleta.2018.03.006>
236. Z.X. Liu et al., *Nucl. Fusion* **60**, 122001 (2020). <https://doi.org/10.1088/1741-4326/abb146>
237. T. Zhang et al., *Plasma Sci. Technol.* **20**, 115101 (2018). <https://doi.org/10.1088/2058-6272/aac9b5>
238. Y.Q. Chu et al., *Plasma Physics Controlled Fusion* **63**, 105003 (2021). <https://doi.org/10.1088/1361-6587/ac1b1f>
239. M. Xu et al., *Chin. Phys. Lett.* **38**, 085201 (2021). <https://doi.org/10.1088/0256-307X/38/8/085201>
240. M. Xu et al., *Nucl. Fusion* **59**, 084005 (2019). <https://doi.org/10.1088/1741-4326/ab2686>
241. X. Han et al., *Nucl. Fusion* **62**, 064005 (2022). <https://doi.org/10.1088/1741-4326/ac5c75>

### Publisher's Note

Springer Nature remains neutral with regard to jurisdictional claims in published maps and institutional affiliations.